Examination of Aerosol Indirect Effects during Cirrus Cloud Evolution

Flor Vanessa Maciel[1], Minghui Diao[1], Ryan Patnaude[1,2]

[1]Department of Meteorology and Climate Science, San Jose State University, San Jose, 95192, USA
5 [2]*Current affiliation:* Department of Atmospheric Science, Colorado State University, Fort Collins, 80521, USA

Correspondence to: Minghui Diao (minghui.diao@sjsu.edu)

Abstract. Aerosols affect cirrus formation and evolution, yet quantification of these effects remain difficult based on in-situ observations due to the complexity of nucleation mechanisms and large variabilities in ice microphysical properties. This work employed a method to distinguish five evolution phases of cirrus clouds based on in-situ aircraft-based observations from
10 seven U.S. National Science Foundation (NSF) and five NASA flight campaigns. Both homogeneous and heterogeneous nucleation were captured in the 1-Hz aircraft observations, inferred from the distributions of relative humidity in the nucleation phase. Using linear regressions to quantify the correlations between cirrus microphysical properties and aerosol number concentrations, we found that ice water content (IWC) and ice crystal number concentration (Ni) show strong positive correlations with larger aerosols (> 500 nm) in the nucleation phase, indicating strong contributions of heterogeneous
15 nucleation when ice crystals first start to nucleate. For the later growth phase, IWC and Ni show similar positive correlations with larger and smaller (i.e., > 100 nm) aerosols, possibly due to fewer remaining ice nucleating particles in the later growth phase that allows more homogeneous nucleation to occur. Both 200-m and 100-km observations were compared with the nudged simulations from the National Center for Atmospheric Research (NCAR) Community Atmosphere Model version 6 (CAM6). Simulated aerosol indirect effects are weaker than the observations for both larger and smaller aerosols. Observations
20 show stronger aerosol indirect effects (i.e., positive correlations between IWC, Ni and Na) in the Southern Hemisphere (SH) compared with the Northern Hemisphere (NH), while the simulations show negative correlations in the SH. The simulations underestimate IWC by a factor of 3 – 30 in the early/later growth phase, indicating that the low bias of simulated IWC was due to insufficient ice particle growth. Such hypothesis is consistent with the model biases of lower frequencies of ice supersaturation and lower vertical velocity standard deviation in the early/later growth phases. Overall, these findings show
25 that aircraft observations can capture the competitions between heterogeneous and homogeneous nucleation, and their contributions vary as cirrus clouds evolve. Future model development is also recommended to evaluate and improve the representation of water vapor and vertical velocity on the sub-grid scale to resolve the insufficient ice particle growth.

Atmospheric
Chemistry
and Physics
Discussions
Open Access

1 Introduction

Cirrus clouds have varying radiative effects, depending on their microphysical properties such as ice water content (IWC), ice
crystal number concentration (Ni) and mean diameter (Di) (Liou, 1992). As a result, the combined shortwave and longwave
radiative effects of cirrus clouds have large spatial and temporal variabilities and may lead to either a warming or cooling
effect on Earth's surface (Fu and Liou, 1993; Liou, 1986). Although cirrus clouds are ubiquitous in the atmosphere, covering
approximately 20% - 40% of Earth's surface at any given time (Mace and Wrenn, 2013; Sassen et al., 2008), the processes
that control their formation and evolution are spatially diverse. These processes range from the microphysical scale, such as
the ice-nucleating properties of both anthropogenic and natural aerosols, to the larger dynamical scale, such as atmospheric
circulations (Pruppacher and Klett, 2010). Because of the complexity of these processes, climate models have difficulties
simulating them accurately and large uncertainties surrounding cirrus characteristics and the related aerosol indirect effects
still exist (e.g., Boucher et al., 2013; Fan et al., 2016; Heymsfield et al., 2017; Kärcher, 2017; Lynch et al., 2002).

Cirrus clouds exist mostly within the upper troposphere and are composed of ice crystals. They can be formed through two
primary mechanisms: heterogeneous nucleation and homogeneous freezing, whereas the former mechanism requires the
presence of ice nucleating particles (INP) to initiate an ice nucleation event and the latter does not (Pruppacher and Klett,
2010). According to Kärcher et al. (2022), during cirrus cloud formation, a competition for available water vapor between
heterogeneous nucleation on INPs and homogeneous freezing of liquid aerosols often occurs. They found that heterogeneous
nucleation can deter the activation of homogeneous freezing as well as reducing the number of ice crystals formed via
homogeneous freezing. Many unknowns still exist regarding the dominance and competitions between these two nucleation
mechanisms. The previous work by Cziczo et al. (2013) showed that heterogeneous nucleation is likely the dominant nucleation
mechanism based on in-situ observations of ice residuals sampled from cirrus in the midlatitudes. However, it is unclear if
similar conclusions would be reached if other geographical locations are examined. Through the use of analytical equations,
Kärcher and Jensen (2017) discovered that cirrus cloud homogeneous freezing is spatially limited and very fleeting, and the
number of ice crystals that are nucleated is affected by both strong diffusion and turbulence. Their findings indicate that a large
dataset of high-resolution observations with measurements of thermodynamic and dynamical conditions would be helpful to
understand the competition between different nucleation mechanisms.

Examination of the nucleation mechanisms is further complicated by the large variabilities seen in cirrus microphysical
properties, associated with cirrus evolution, thermodynamic/dynamic conditions, aerosol indirect effects, and geographical
variations. Using aircraft observational data, O'Shea et al. (2016) found that in an actively growing cirrus cloud case with
strong updrafts, ice crystal number concentration (Ni) was much higher compared with a decaying cirrus case by a factor of
10, and the decaying case had fewer particles larger than 700 μm. Using data from 28 flights across the arctic, midlatitudes,
and tropics, Krämer et al. (2009) observed low Ni in certain cirrus clouds, which may be responsible for the elevated and
persistent ice supersaturations detected inside cirrus clouds. Here, ice supersaturation (ISS) is defined as where relative
humidity with respect to ice (RHi) is greater than 100%. By acting as cloud condensation nuclei (CCN) and/or ice nucleating

particles (INPs), aerosols affect cloud properties and radiation (Bruce, 1989; Lohmann and Feichter, 2005; Twomey, 1977). Patnaude and Diao (2020) isolated aerosol indirect effects on cirrus clouds by restricting other conditions (e.g., thermodynamic and dynamic) and found increasing ice water content (IWC) and Ni with increasing aerosol number concentrations (Na) based on multiple flight campaigns. Using satellite observations, Zhao et al. (2019) found that near cloud top in convective systems, the effects of polluted continental aerosols on ice particle effective radius vary between strong and moderate convective systems. Another study used aircraft data from the Interhemispheric Differences in Cirrus Properties from Anthropogenic Emissions (INCA) campaigns and showed that cirrus clouds in the Northern Hemisphere (NH) had higher Ni and lower effective diameters when compared with cirrus clouds in the Southern Hemisphere (SH) (Gayet et al., 2004). Based on the distributions of RHi from INCA campaigns, Haag et al. (2003) found that cirrus clouds in the SH midlatitudes are more likely to form by homogeneous freezing compared with NH midlatitude cirrus, indicating a possible role of aerosol indirect effects for controlling the in-cloud RHi distributions and the nucleation thresholds.

Several methods have been developed to compare high-resolution in-situ observations with coarser scale simulations of global climate models (GCMs). Patnaude et al. (2021) compared an in-situ observational dataset with National Center for Atmospheric Research (NCAR) Community Atmosphere Model version 6 (CAM6) simulations and found an underestimation of IWC by a factor of 3 to 10 in the NH and SH (except for SH midlatitudes), as well as weaker aerosol indirect effects in the simulations. Eidhammer et al. (2014) compared in-situ observations with CAM5 and found that simulated ice crystals have inaccurate size distributions. Using an updated CAM6 version with black carbon (BC) treated as INPs, McGraw et al. (2020) found a thinning effect followed by a thickening effect on cirrus as BC concentration increases. These studies show the importance of understanding cirrus cloud microphysical properties and aerosol indirect effects based on observations and simulations. However, a knowledge gap still exists regarding the aerosol indirect effects on different evolution phases of cirrus clouds especially during ice nucleation and growth.

In this work, we conducted an observation-based analysis using global-scale airborne in-situ measurements in order to understand the variations of cirrus microphysical properties and aerosol indirect effects at various geographical locations. In addition, the representation of these properties and processes in a GCM – NCAR CAM6 – was evaluated. We applied the method of Diao et al. (2013) to derive various evolution phases of cirrus clouds, which enables a detailed examination of aerosol indirect effects from nucleation to early growth and later growth phase. Comparisons between observational and simulated data were conducted through a scale-aware method, targeting cirrus microphysical properties, i.e., IWC, Ni, and mean diameter (Di), and aerosol indirect effects. In section 2, we describe the observational datasets and model simulations used for this study. In section 3, We describe the statistical distributions of IWC, Ni and Di in relation to temperature and Na at various geographical locations. Section 4 discusses the implications of observed features and model biases.

2 Observational and Simulation Datasets

2.1 In-situ observations from multiple flight campaigns

For this study, we used a global-scale observational dataset comprising of seven U.S. National Science Foundation (NSF) and five NASA campaigns. The campaign name, time, location, and flight hours of the NSF campaigns are listed in Table 1. Figure

95   1 a and b depict the flight tracks for the NSF and NASA campaigns for the conditions of temperatures ≤ -40°C, respectively. We excluded measurements at temperatures > -40°C for our analysis to eliminate the existence of supercooled liquid water. These campaigns provide wide-ranging spatial coverage, spanning latitudinally from 87°N to 75°S and longitudinally from 128°E to 38°W, from the surface to the upper troposphere and lower stratosphere.

The acronyms of NSF campaigns are listed alphabetically as follows: CONTRAST (Pan et al., 2017), DC3 (Barth et al., 2015),

100 HIPPO (Wofsy, 2011), ORCAS (Stephens et al., 2018), PREDICT (Montgomery et al., 2012), START08 (Pan et al., 2010), and TORERO (Volkamer et al., 2015). Data were collected by instruments aboard the NSF/NCAR High-Performance Instrumented Airborne Platform for Environmental Research (HIAPER) Gulfstream V (GV) research aircraft. The data are composed of 1-Hz observations of meteorological parameters such as temperature, water vapor, N_a, vertical velocity (w) and cloud microphysical properties (i.e., IWC, N_i, D_i). Water vapor measurements are provided by the Vertical Cavity Surface

105 Emitting Laser (VCSEL) hygrometer aboard the aircraft (Zondlo et al., 2010). The saturation vapor pressure with respect to ice ($e_{s,ice}$) was calculated following the equation in Murphy and Koop (2005). RHi was further computed by using the water vapor mixing ratio, pressure and temperature. We used the ice crystal measurements collected by the Fast Two-Dimensional Cloud Probe (Fast-2DC) (62.5 – 3200 µm). Aerosol measurements ranging from 60 to 1000 nm were obtained by the Ultra-High Sensitivity Aerosol Spectrometer (UHSAS), which uses 99 logarithmically-spaced bins to measure their concentration

110 and size distribution. The first deployment for HIPPO was excluded due to the absence of ice particle measurements. START08 campaign did not have aerosol measurements and was not used in the analysis of aerosol indirect effects.

Five NASA-funded aircraft campaigns are also included in this work to compare with NSF observations, including the ATTREX, MACPEX, DC3, POSIDON, and SEAC4RS campaigns (full names shown in Table 1). The main purpose of the analysis of these NASA campaigns is to provide a contrast to the NSF data from different airborne platforms and

115 instrumentations, such as the ice crystal measurements collected by the 2D-S Stereo Probe (2DS) (5 – 3005 µm) and water vapor measurements collected by the Diode Laser Hygrometer (DLH). In addition, we applied extensive quality control to this merged observational dataset. Table S1 in the accompanying Supplement shows the UTC timestamps that were filtered out with a comment on the specific measurements found problematic.

For the merged datasets, ice supersaturated regions (ISSR) and ice crystal regions (ICR) were identified using values of RHi

120 and N_i, respectively. ISSRs are regions where the RHi is above 100%. ICRs are regions where in-cloud conditions are consecutively detected. The 1-Hz samples with at least one ice particle detected is defined as in-cloud regions. The remaining regions are defined as clear-sky conditions. We employ the method established in Diao et al. (2013), which uses the spatial ratios of ISSR and ICR to identify instances of the five evolution phases of cirrus clouds within the in-situ observations. These

phases are categorized as: (1) clear-sky ISSRs, (2) nucleation, (3) early growth of ice crystals, (4) later growth of ice crystals,

125   and (5) sedimentation/sublimation. Figure 2 shows an idealized illustration of these five evolution phases. One should note that these idealized phases may appear simultaneously in the same cloud, and the time evolution may not follow the exact sequence from phase 1 to 5. These phases may also be adjacent or overlap with each other in a 3-D view, but may not be captured from 1-D sampling of in-situ airborne observations. To compare the high-resolution NSF observational data with the coarse-resolution model data, a running average of 430 seconds was applied to the 1-Hz observation data. This timescale, i.e.,

130   430 seconds, was chosen since it converts to a horizontal scale of about 100 km for a mean air speed of 230 m s^{-1} for all campaign data with a temperature less and equal to -40°C. To calculate the average IWC and Ni, the 430 seconds include both in-cloud and clear-sky conditions. For phase identification, the 430-second averaged data continued to use the center point phase identifications that were originally assigned to the 1-Hz data. This is because the evolution phase identification relies on using high-resolution observations to capture the transitioning between ICRs and ISSRs.

135   **2.2 CESM CAM6 model simulations**

We conducted nudged simulations of the NCAR CAM6 model for each of the seven NSF flight campaigns. Model output collocated with their respective flight tracks was saved and used in the analysis. The specific configuration of the model simulation is identical to that in Patnaude et al. (2021). These simulations were nudged for temperature and 2-D horizontal wind according to the Modern-Era Retrospective Analysis for Research and Applications version 2 (MERRA2) data (Gelaro

140   et al., 2017). All seven simulations had a spin-up time of 6-months before their respective campaign's start date. These simulations have 32 vertical levels and a horizontal resolution of 0.9 degrees by 1.25 degrees. When selecting the nearest model output to the one-dimensional flight track in vertical, we use the model vertical level with the closest temperature to the observations.

Similar to the observational data, the $e_{s,ice}$ is calculated using the Murphy and Koop (2005) equation, while the RHi was

145   determined from the temperature and specific humidity. In addition, by applying the methods from Eidhammer et al. (2014), we restricted the simulated ice and snow to ≥ 62.5 µm, which is the size cut-off for the Fast-2DC probe. The mass and number concentrations of ice and snow were then calculated by using the integrals of incomplete gamma functions from 62.5 µm to 3200 µm. After applying this size restriction, simulated IWC, Ni and Di were calculated by combining the ice and snow variables for the comparisons with the in-situ observations of cirrus clouds. Mass concentrations ("IWC" and "QSNOW") and

150   number concentrations ("NUMICE" and "NSNOW") of ice and snow are summed up, respectively. Total aerosol number concentration was calculated by adding the Aitken, accumulation, and coarse aerosol mode concentrations, which were size-restricted to reflect the UHSAS measurement range. Using this method, the simulated Na_{100} and Na_{500} were calculated, which represent number concentrations of aerosols larger than 100 nm and 500 nm, respectively. Since the coarse-scale grid box of a GCM cannot capture the high-resolution spatial relationships between ISSRs and ICRs, the method of identifying five

155   evolution phases of cirrus clouds cannot be applied on the 1-degree grid box scale. However, since only collocated model output to the 1-D flight track is used in this analysis, the comparison between each observation datum and its nearest model

point assumes that the model point has the same cirrus evolution phase as that specific observation datum. In other words, we assume that the model output has the same cloud evolution phase as the matching observations and then evaluate the associated cirrus microphysical properties and aerosol indirect effects for each phase.

160 **3 Results**

3.1 Occurrence frequencies of five cirrus evolution phases

The probabilities of ICR/ISSR spatial ratios for each campaign and various latitudinal regions are shown in Figure 3 a – c. This parameter allows us to quantify how ICRs expand with respect to ISSRs. In Figure 3 a and b, the ICR/ISSR spatial ratio almost always peaks around one for each campaign, meaning that ICRs and ISSRs often have similar spatial scales in each

165 cloud segment, which suggests that these regions are likely to coexist. The combined NSF and NASA data were further separated into six latitudinal regions: Northern Polar (NP), Northern Midlatitude (NM), Northern Tropical (NT), Southern Polar (SP), Southern Midlatitude (SM), and Southern Tropical (ST) to investigate possible hemispherical differences in cirrus cloud properties (Figure 3 c). Similar to the analysis of each campaign, ICR/ISSR spatial ratios peak at one for most of the latitudinal regions.

170 Using the ICR/ISSR ratios, five evolution phases are identified for all flight campaigns, and their probabilities are shown in Figure 3 d – f. The result shows that a cloud segment has the highest probability to be in the early growth phase (i.e., phase 3) for almost all the campaigns (except MACPEX). When separated by latitudinal regions, evolution phase 3 consistently shows the highest probability for most regions. Note that the method of counting the number of points for various evolution phases in this study is based on the number of seconds of observations, instead of the number of consecutive segments as shown in

175 Diao et al. (2013, 2014b). The previous studies by Diao et al. (2013, 2014b) showed higher probabilities of phases 1 and 5 because most of these phases have more cases but shorter lengths.

Occurrence frequencies of clear-sky ISS have been previously used as an indicator of ice nucleation (e.g., Ovarlez et al., 2002; Diao et al., 2014b). That is, lower clear-sky ISS frequencies indicate that ISSRs are more likely to transition into ICRs and ice nucleation is more likely to occur. This study found that NH has lower clear-sky ISSR frequencies (0.16) compared with the

180 SH (0.28) when counting the total seconds of samples. Diao et al. (2014b) found similar frequencies of clear-sky ISSRs between the NH and SH (their Figure 5) when comparing the number of consecutive segments. These two findings indicate that clear-sky ISSR segments in the NH are patchier than those in the SH. In addition, the ORCAS campaign located around Punta Arenas, Chile, is around the same region as the southbound flights of INCA campaign. The ORCAS campaign shows the highest clear-sky ISSR frequency among all NSF and NASA campaigns (Figure 3 d), which may be the reason that this

185 work and the previous work of Ovarlez et al. (2002) both show higher clear-sky ISS frequencies in the SH.

Examining each latitudinal region, NM and NT have lower frequencies of clear-sky ISSRs (i.e., phase 1) compared with their counterparts in the SH. This is likely due to the higher aerosol loading in the NM and NT, resulting in an earlier activation of ice nucleation and lower ice supersaturation frequency. For the polar regions, both NP and SP have relatively higher

190 frequencies of clear-sky ISSRs (frequencies of 0.6 and 0.35, respectively). The higher ice supersaturation frequencies in the polar regions were also previously observed in satellite data (e.g., Gettelman et al., 2006). NP has higher frequencies of clear-sky ISSRs than the SP, possibly due to the asymmetrical sampling of more higher latitudes in the NH than the SH (as shown in Figure 2 c and d).

3.2 Relative humidity and particle size distributions for each evolution phase

Distributions of RHi for each phase and all evolution phases are shown in Figure 4. As cirrus clouds evolve from clear-sky

195 ISSRs to regions with both ice crystals and ice supersaturation, the RHi first increases with ISSR length for phase 1 before the first ice crystals appear, but decreases with the spatial ratio of ICR/ISSR once ice crystal formation and growth reduces the amount of available water vapor exceeding ice saturation. Subsequently, as ice particles sediment and sublimate, the decreasing ICR lengths are associated with decreasing RHi, indicating that more ice particles sediment into drier conditions as the cirrus evolves in this final phase. As a result, phase 5 also has the widest range of RHi values during sedimentation and sublimation

200 compared with other phases. Interestingly, the highest RHi values are mostly seen in phase 2 (nucleation phase) instead of phase 1 (clear-sky ISSR), indicating that phase 2 is a better representation of the RHi threshold for ice nucleation compared with phase 1. The maximum RHi values seen in phases 1 and 2 from seven NSF campaigns are 173% and 174%, while those seen in NASA campaigns are 180% and 212%, respectively. Since the RHi threshold of homogeneous freezing calculated based on 0.5 µm aerosols ranges from 140% to 160%, this result indicates that homogeneous freezing has been observed and

205 can be captured in the nucleation phase identified from the method represented here. However, since most (89%) of the nucleation phase (red markers) have RHi values less than 140% among all ice supersaturated conditions, it suggests that heterogeneous nucleation mechanism is likely the more commonly observed mechanism for ice nucleation compared with homogeneous freezing. Similar method of using the RHi distribution to indicate the dominant nucleation mechanisms of cirrus clouds from in-situ airborne observations was used by Cziczo et al. (2013). Yet this study is the first one to directly separate

210 the nucleation phase from in-situ airborne observations and examines the RHi distribution only for the nucleation phase.

Hemispheric distributions of the five evolution phases and their frequencies of showing ISS exceeding 40% among all ISS conditions are shown in Figure 5. This analysis uses the combined dataset of NSF and NASA campaigns. Frequencies of each evolution phase are calculated by the number of samples (in seconds) of a certain phase in a specific bin divided by the total number of samples (in seconds) in that bin. The tropical regions show higher frequencies of the later growth phase (phase 4),

215 indicating that cirrus clouds in the tropics may have prolonged lifetime with sustained availability of excess water vapor over ice saturation. The SH midlatitudes have slightly higher frequencies of clear-sky ISSRs compared with the NH midlatitudes, possibly due to higher concentrations of INPs in the NH midlatitudes. The frequencies of high RHi (> 140%) are calculated by the number of samples of RHi > 140% divided by the number of samples of RHi > 100%. Higher RHi values were observed more frequently in phase 2 in the NH and SH extratropical regions. Most bins in phase 2 show less than 0.1 frequencies for

220 RHi exceeding 140% among all ice supersaturated conditions, indicating that heterogeneous nucleation is more dominant than homogeneous freezing in the nucleation phase.

Number concentrations of ice particles in various size bins are examined by using the particle size distribution (PSD) plots for the NSF and NASA datasets in Figure 6, separated by various campaigns, latitudes, and evolution phases. The 2DC and 2DS probes were used in NSF and NASA data, respectively. For NSF data, the DC3 campaign shows the highest particle number
225 concentrations per bin while ORCAS has the lowest. This may be because DC3 primarily targeted anvil outflows from convective systems over the central U.S., while ORCAS sampled in-situ formed cirrus clouds over the Southern Ocean region. Convective cirrus is often seen to be associated with higher IWC and Ni (e.g., Krämer et al., 2016) compared with in-situ observations. In addition, the higher Na in the continental U.S. compared with the Southern Ocean also generally leads to higher total Ni as seen in Patnaude and Diao (2020). Similar features are seen in NASA campaigns, that is, NASA DC3 has
230 the highest particle number concentration per bin while ATTREX has the lowest. This is consistent with the fact that ATTREX mostly sampled the western Pacific Ocean region. Latitudinal variations in PSD are examined in Figure 6 c and d. For the NSF data, the NH has higher particle number concentrations per bin compared with its counterparts in the SH. A consistent result is seen in the NASA data with higher concentrations per bin in the NT compared with ST.

When separated by evolution phases (Figure 6 e and f), among the three phases that ice particles coexist with ice supersaturation
235 (phases 2 – 4), the nucleation phase (phase 2) shows the lowest particle number concentration per bin for both NSF and NASA data. In addition, the later growth phase (phase 4) shows the highest particle number concentration per bin when the size is less than 1700 µm, likely due to continuous ice crystal formation and growth with a sufficient supply of water vapor. The previous study of Diao et al. (2013) also observed an increasing Ni along the time evolution of cirrus clouds, while Spichtinger and Gierens (2009) showed similar increasing Ni trend along cirrus evolution using a box model.

240 **3.3 Comparisons of cirrus microphysical properties between observations and simulations**

The relationships of $\log_{10}$(IWC), $\log_{10}$(Ni) and Di with respect to temperature are shown for each of the in-cloud evolution phases (2 – 5) for 1-s observations, 430-s averaged observations and CAM6 simulations in Figure 7. For both higher and lower resolution observations, phase 4 shows the higher IWC and Ni, followed by phase 3, phase 5 and phase 2, demonstrating that IWC and Ni continue to increase from nucleation phase to later growth phase but decrease as the evolution proceeds to
245 sedimentation/sublimation. This trend is consistent with the analysis of PSD (Figure 6) as well as the previous study of Diao et al. (2013). CAM6 simulations are able to capture the same evolution trend of IWC and Ni as the observations. The model also captures the increasing trend of IWC, Ni and Di with increasing temperature as seen in the observations.

One of the main differences between the simulations and observations is the much lower simulated IWC in phases 3 and 4 (early and later growth phases) by 0.5 and 1–1.5 orders of magnitude, respectively. The lower IWC seen in the model has also
250 been shown in Patnaude et al. (2021). In addition, the model shows smaller variations of IWC and Ni between the nucleation phase and later growth phase compared with the observations, indicating insufficient growth of ice particles after ice nucleation. For both observations and simulations, Di does not show significant variations among different evolution phases. However, the simulated Di is lower than observed values by a factor of 1.5 – 2 for all phases.

3.4 Aerosol indirect effects and nucleation mechanisms during cirrus evolution

255   The relationships between aerosol concentrations (Na) and cirrus microphysical properties are examined for smaller and larger aerosols (Figures 8 and 9, respectively). Both 1-s and 430-s observations show increasing IWC and Ni with increasing Na_{100}, indicating aerosol indirect effects of smaller aerosols (> 100 nm) for facilitating ice crystal formation. Compared with Na_{100}, Na_{500} shows the most significant positive correlations with IWC and Ni for the nucleation phase especially at $Na_{500} > 2$ cm^{-3} (i.e., $\log_{10}Na_{500} > 0.3$), followed by the early growth phase, then later growth phase. This result indicates that large aerosols (>

260   500 nm) likely act as INPs to initiate ice nucleation, and heterogeneous nucleation occurs frequently during the nucleation phase in the observations. Compared with the observations, simulations do not show a significant trend of cirrus microphysical properties in relation to either Na_{100} or Na_{500}.

Similar to Figure 7, both 1-s and 430-s observations show a similar trend of increasing IWC and Ni as cirrus evolves from phase 2, 3 to 4. An interesting difference between Na_{100} and Na_{500} is seen for their impacts on the nucleation phase, that is,

265   IWC and Ni seem to reach relatively constant values when Na_{500} exceeds 20 cm^{-3} (i.e., $\log_{10}Na_{500} > 1.3$), while the IWC and Ni continue to increase with Na_{100} throughout the entire range of Na_{100}. This feature indicates that as Na_{500} exceeds a threshold, the available INPs in the air parcel may have been depleted, and therefore no new ice nucleation can be initiated with additional larger aerosols that are not INPs. On the other hand, increasing number concentrations of smaller aerosols (Na_{100}) likely contribute to more homogeneous freezing since the homogeneous freezing is less dependent on the aerosol composition as the

270   heterogeneous nucleation is.

Differing from the observations, the simulated IWC is almost identical among various cirrus evolution phases at various Na_{100} bins, while the simulated Ni shows slightly lower Ni for the nucleation phase (phase 2). The missing variations among different evolution phases are likely caused by two factors – one is the insufficient growth of ice particles after ice nucleation as discussed for Figure 7; the other is the weaker correlations between Na and temperature in the simulations compared with

275   observations (Figure S1 in the Supplement). The observed Na_{100} and Na_{500} both positively correlate with temperature, yet these correlations are weaker in the model. As a result, when examining evolution phases in relation to Na_{100}, each Na_{100} bin in the simulation may contain a wider range of temperatures compared with the observations, while the observations binned by Na_{100} have better constraints on temperature.

To quantify aerosol indirect effects on cirrus microphysical properties, linear regressions were applied to the 1-s observations,

280   430-s observations and model simulations (Figures 10 and 11). Differing from Figures 8 and 9, delta values were calculated by subtracting the average values of the corresponding 1-degree temperature bin from the individual datum. The delta values were calculated for logarithmic IWC, Ni, Di, Na_{100} and Na_{500}. Patnaude and Diao (2020) showed that restricting the temperature influence before quantifying aerosol indirect effects is very important as the temperature can be a major factor affecting cirrus microphysical properties. Thus, delta values are also used in this study to minimize the impact of temperature when analyzing

285   aerosol indirect effects. Table S2 in the Supplement documents the full linear regression equations, including slopes, intercepts, and their standard deviations. After restricting the temperature influences, positive correlations are seen for IWC and Ni with

respect to both Na_{100} and Na_{500} for all phases with ice supersaturation (i.e., phases 2 – 4) in the 1-s observations. For the 430-s observations, positive correlations are also seen for phases 3 and 4, but the correlations become insignificant for phase 2. This is due to the spatial averaging process that includes clear-sky segments as part of the grid averages. Since phase 2

290 (nucleation phase) generally has shorter lengths of ICRs compared with phases 3 and 4 (as shown in Figure 4), the averaging process leads to lower IWC and Ni for phase 2 compared with phases 3 and 4. Due to this reason and the fewer samples of phase 2, the distributions of IWC and Ni also show more fluctuations in the coarser scale observations.

Aerosol indirect effects on IWC and Ni are quantified by the slope values of linear regressions (given in the figure legend). The slope values between IWC and Ni are comparable with each other for the observations on the same scale (e.g., Figure 10

295 a and d, b and e), but show lower values for 430-s observations compared with 1-s observations. Nevertheless, the positive slope values are consistently seen for phases 3 and 4 between 1-s and 430-s observations against both Na_{100} and Na_{500}. Compared with observations, the simulations show either negative correlation or no significant correlation with respect to Na_{100}. As for the impact of Na_{500}, the simulations show a slight positive correlation between Ni and Na_{500} in phase 4 (later growth phase), but a negative correlation is seen for phase 2 (nucleation phase). This result indicates that the model may have

300 weaker aerosol indirect effects from larger aerosols to activate ice nucleation than those seen in the observations.

Contrasting the role of smaller and larger aerosols based on high-resolution observations, the smaller aerosols show the strongest positive correlations with IWC and Ni in phase 4. On the contrary, the larger aerosols show the strongest correlations with these properties in phase 2. This feature suggests that when ice nucleation just starts to occur, the larger aerosols which often include INPs likely dominate ice nucleation in the nucleation phase. The dominance of heterogeneous freezing on the

305 nucleation phase can be seen from the slope values of IWC and Ni, i.e., 1.2 and 0.98 with respect to Na_{500}, which are about 3.6 – 3.8 times of the slope values of 0.33 and 0.26 with respect to Na_{100}, respectively.

As cirrus evolve with additional ice supersaturation, more ice nucleation events start to take place possibly with similar amounts of contributions from homogeneous freezing and heterogeneous nucleation. The comparisons of two nucleation mechanisms are illustrated in the slope values of IWC and Ni for phase 4, that is, 0.43 and 0.16 with respect to Na_{500}, similar

310 to the slope values of 0.41 and 0.23 with respect to Na_{100}, respectively. This feature is likely caused by a gradual depletion of INPs in the previous nucleation events through heterogeneous nucleation unless a continuous supply of new INPs is available, resulting in comparable contributions from both nucleation mechanisms.

3.5 Latitudinal variations of aerosol indirect effects on cirrus clouds

A further investigation on the variations of cirrus microphysical properties during their evolution is conducted for different

315 latitudinal regions: the tropics, midlatitudes and polar regions in the NH and SH (Figure 12). The geometric means of IWC, Ni and linear averages of Di at various temperatures are shown for phases 2+3+4 (i.e., phases with ice supersaturation, top three rows) and sedimenting phase 5 (bottom three rows). The largest hemispheric differences in IWC and Ni for all phases 2 – 5 are seen in the midlatitudes, with about 1–2 orders of magnitude of higher IWC and Ni in the NH than SH based on 1-s and 430-s observations. The simulations also capture the hemispheric differences in the midlatitudes, but only show 0.5 order

320 of magnitude of difference. Different from the midlatitudes, the polar regions show higher Di in the SH, while the tropics do not show significant hemispheric differences.

The aerosol indirect effects are contrasted between the NH and SH by combining phases 2 – 4 (Figure 13). Comparing the two hemispheres, the 1-Hz observations show stronger aerosol indirect effects on IWC and Ni in the SH (i.e., larger slope values for the positive correlations) compared with the NH. The stronger aerosol indirect effects are seen from both smaller and larger

325 aerosols, indicating that increasing aerosol concentrations in the SH may be more effective in increasing ice nucleation compared with the NH. Similar to Figures 10 and 11, model simulations show weaker aerosol indirect effects compared with observations for the NH, and the model even shows negative correlations for IWC and Ni with respect to Na_{100} and Na_{500} in the SH. Whether this model bias is caused by the inaccurate representations of INPs or aerosol indirect effects in the two hemispheres needs more investigation in future studies.

330 **3.6 Diagnosis of model biases due to thermodynamic and dynamic conditions**

The model limitations in the representations of cirrus microphysical properties at various evolution phases are assessed by their thermodynamic and dynamic conditions in Figures 14 and 15, respectively. Figure 14 examines the distributions of RHi in relation to temperature for 1-s observations, 430-s observations, and model simulations. Comparing the two scales of observations, the coarser scale observations show lower magnitude of ice supersaturation for phases 1–4, due to the spatial

335 averaging that smooths the fluctuations of RHi. The simulations show lower frequency of ice supersaturation compared with the 430-s observations, even though the maximum RHi is similar between the simulations and the 430-s observations. That is, the model simulations show 28%, 25%, 31%, and 31% of the total samples above ice saturation for phases 1 – 4, respectively. The 1-s observations show 100%, 100%, 63%, and 45%, respectively. The 430-s observations show 49%, 50%, 45%, and 27%, respectively. The lower frequency of ice supersaturation likely leads to the lower IWC seen in the early and later growth

340 phases (Figure 7).

Figure 15 shows the distribution of vertical velocity (w) in relation to RHi for various datasets. To better compare with model results, σ_w, or standard deviation of w, is calculated for every 40 seconds or 430 seconds of observations. The σ_w values from the observations are compared with the model output variable w_{sub}, similar to the previous method by Patnaude et al. (2021). The 1-s observations show higher σ_w values compared with 430-s observations, and the highest σ_w values are seen around 4

345 m/s and 3 m/s for 1-s and 430-s observations, respectively. The model simulations show maximum σ_w values around 1 m/s, much lower than the observations. 90% of the 1-Hz observations, 430-s observations, and simulation data show σ_w values lower than 0.54, 0.63, 0.052 m/s, respectively. Low biases in the simulated σ_w values were also seen in Patnaude et al. (2021). Both the lower σ_w values and lower ice supersaturation frequencies can contribute to the lower IWC in the model.

Atmospheric
Chemistry
and Physics
Discussions

4 Discussion and Conclusions

350 Cirrus clouds affect radiation budget significantly with their ubiquitous coverage and vertical locations at high altitudes. In a changing climate, it is imperative to improve the understanding of cirrus cloud formation, evolution, and their relationship with aerosols. This study provides a first look of aerosol indirect effects on various evolution phases of cirrus clouds based on the method of Diao et al. (2013), by using multiple flight campaigns and global climate model simulations.

The contributions of heterogeneous and homogeneous nucleation have been inferred from two types of analyses, including
355 RHi distributions with respect to temperature and aerosol indirect effects using linear regressions. Both analyses have been separated into five evolution phases, with a specific target on phases 2 – 4 when ice supersaturation is available, that is, nucleation, early growth, and later growth phases. The RHi distributions for phase 2 show the highest magnitude (~160% to 180%) compared with phase 1 (clear-sky ice supersaturation), indicating that in-situ, high-resolution (1-Hz) airborne observations are capable of capturing homogeneous freezing, even though this mechanism was shown to be transient and
360 small-scale based on model simulations (Kärcher and Jensen, 2017). Using the slope values to quantify correlations of IWC and Ni with respect to Na (either Na_{100} or Na_{500}), the nucleation phase shows strong positive correlations with Na_{500}, indicating a dominant contribution from heterogeneous nucleation. Comparatively, phase 4 shows positive correlations of IWC and Ni in relation to both Na_{500} and Na_{100} with similar slope values, indicating similar contributions from two nucleation mechanisms for the later growth phase. This evolving weight of contribution from two nucleation mechanisms indicates that one nucleation
365 mechanism may not dominate over the entire lifetime of a cirrus cloud, but rather part of its evolution.

Several main model limitations have been identified, including lower IWC and Di, and weaker aerosol indirect effects. For the underestimation of IWC and Di in the model, Patnaude et al. (2021) has previously identified this issue but did not provide an investigation on whether such underestimation is caused by the lack of ice nucleation events or ice crystal growth. In this work, after separating five evolution phases, phases 2 and 5 (nucleation and sedimentation) show no significant biases in the
370 simulated IWC, yet phases 3 and 4 (early and later growth) show large underestimation of IWC in the simulations. This result indicates that the simulated IWC is mainly lower due to the lack of ice particle growth instead of insufficient ice nucleation. This feature is corroborated by the lower frequency of ice supersaturation and lower magnitudes of vertical velocity fluctuations seen in phases 3 and 4 in the simulations (Figures 14 and 15, respectively). The other main issue of weaker aerosol indirect effects in the simulations could be caused by either an insufficient amount of INPs considered in the model, or by the
375 lower local ice supersaturation within each grid box at sub-grid scale. Previously, Diao et al. (2014a) showed that ice supersaturation occurs frequently at the scale of hundreds of meters, which is much lower than the GCM grid scale. Thus, future model development is recommended to investigate the representation of sub-grid scale RHi and w in order to allow sufficient thermodynamic and dynamic conditions for ice nucleation. In addition, more investigation is warranted to examine the types of aerosols that could be potentially lacking in the GCM as INPs.

380 Comparisons among various latitudinal regions have been conducted for tropics, midlatitudes and polar regions. The simulations show smaller hemispheric differences in the midlatitudinal regions compared with the observations, possibly due

to weaker aerosol indirect effects. Comparing the two hemispheres, larger and smaller aerosols both show stronger aerosol indirect effects in the SH than the NH. These differences in aerosol indirect effects reflect the different hemispheric distributions of INPs as well as other conditions (thermodynamic and dynamic). Limited by the availability of aerosol
385 composition measurements in these flight campaigns at cirrus altitudes, future studies are recommended to investigate the aerosol indirect effects associated with different aerosol compositions at various geographical locations.

Limitations associated with the cirrus cloud evolution phase identification need to be cautioned. Ice crystals that are generated near ice saturation may be mis-represented between different phases because this method requires the usage of RHi for distinguishing evolution phases, and the RHi measurement uncertainties are around $6\% - 7\%$. In addition, because aircraft in-
390 situ observations only provide 1-D sampling, information about the possible cloud layers above or below the flight track is not available. For instance, ice crystals that fall from higher altitudes into lower-altitude ISSRs may potentially be treated incorrectly as newly formed ice crystals.

Overall, these results show the importance of considering the evolutionary phase of a cirrus cloud when analyzing their microphysical properties and the indirect effects of aerosols. Without separating out the phases, these cloud characteristics
395 represent a mixture of all evolution phases, which have large variations and different responses to aerosols. When analyzing aerosol indirect effects, phase 5 is not recommended to be included as part of the analysis due to the lack of ice supersaturation. This work also demonstrated the application of a global-scale observation datasets by combining multiple flight campaigns with detailed quality control. The variations in geographical locations for cirrus microphysical properties and aerosol indirect effects can be used for evaluation of other GCM simulations. Identification of the discrepancies in cirrus characteristics and
400 the diagnosis of the possible underlying reasons (effects of aerosols, thermodynamic and dynamic conditions) provide a pathway to better parameterize cirrus clouds and the factors influencing them at various spatial scales.

Code availability

The source code to run the CAM6 model simulations used in this work along with the accompanying namelist is stored on NCAR's Cheyenne supercomputer (under /glade/campaign/univ/usjs0006/). Permission to access this code will be provided
405 by the authors on request.

Data availability

Observations from the seven NSF flight campaigns are accessible at https://data.eol.ucar.edu/. Observations from the five NASA flight campaigns are accessible at https://www-air.larc.nasa.gov/missions.html.

Author contributions

410   F. Maciel and M. Diao contributed to the development of the ideas, conducted quality control to aircraft-based observations, and wrote the manuscript. F. Maciel contributed to the subsequent data analysis. R. Patnaude generated all the model simulations.

Competing interests

The authors declare that they have no conflict of interest.

Acknowledgments

415

References

420   Barth, M. C., Cantrell, C. A., Brune, W. H., Rutledge, S. A., Crawford, et al.: The Deep Convective Clouds and Chemistry (DC3) Field Campaign, Bull. Am. Meteorol. Soc., 96, 1281–1309, https://doi.org/10.1175/BAMS-D-13-00290.1, 2015.

Boucher, O., Randall, D., Artaxo, P., Bretherton, C., Feingold, G., Forster, P., Kerminen, V.-M., Kondo, Y., Liao, H., Lohmann, U., Rasch, P., Satheesh, S. K., Sherwood, S., Stevens, B., and Zhang, X.-Y.: IPCC AR5 Clouds and Aerosols, In: Climate Change 2013: The Physical Science Basis. Contribution of Working Group I to the Fifth Assessment Report
425   of the Intergovernmental Panel on Climate Change [Stocker, T.F., D. Qin, G.-K. Plattner, M. Tignor, S.K. Allen, J. Boschung, A. Nauels, Y., 571–658 pp., 2013.

Bruce, A.: Aerosols, Cloud Microphysics, and Fractional Cloudiness, Science (80-.)., 245, 1227–1230, https://doi.org/10.1126/science.245.4923.1227, 1989.

Cziczo, D. J., Froyd, K. D., Hoose, C., Jensen, E. J., Diao, M., Zondlo, M. A., Smith, J. B., Twohy, C. H., and Murphy, D. M.:
430   Clarifying the Dominant Sources and Mechanisms of Cirrus Cloud Formation, Science (80-.)., 340, 1320–1324, https://doi.org/10.1126/science.1234145, 2013.

Diao, M., Zondlo, M. A., Heymsfield, A. J., Beaton, S. P., and Rogers, D. C.: Evolution of ice crystal regions on the microscale based on in situ observations, Geophys. Res. Lett., 40, 3473–3478, https://doi.org/10.1002/grl.50665, 2013.

Diao, M., Zondlo, M. A., Heymsfield, A. J., Avallone, L. M., Paige, M. E., Beaton, S. P., Campos, T., and Rogers, D. C.:

Atmospheric
Chemistry
and Physics
Discussions
Open Access
EGU

435   Cloud-scale ice-supersaturated regions spatially correlate with high water vapor heterogeneities, Atmos. Chem. Phys., 14, 2639–2656, https://doi.org/10.5194/acp-14-2639-2014, 2014a.

Diao, M., Zondlo, M. A., Heymsfield, A. J., and Beaton, S. P.: Hemispheric comparison of cirrus cloud evolution using in situ measurements in HIAPER Pole-to-Pole Observations, Geophys. Res. Lett., 41, 4090–4099, https://doi.org/10.1002/2014GL059873, 2014b.

440   Eidhammer, T., Morrison, H., Bansemer, A., Gettelman, A., and Heymsfield, A. J.: Comparison of ice cloud properties simulated by the Community Atmosphere Model (CAM5) with in-situ observations, Atmos. Chem. Phys., 14, 10103–10118, https://doi.org/10.5194/acp-14-10103-2014, 2014.

Fan, J., Wang, Y., Rosenfeld, D., and Liu, X.: Review of Aerosol–Cloud Interactions: Mechanisms, Significance, and Challenges, J. Atmos. Sci., 73, 4221–4252, https://doi.org/10.1175/JAS-D-16-0037.1, 2016.

445   Fu, Q. and Liou, K.-N.: Parameterization of the Radiative Properties of Cirrus Clouds, J. Atmos. Sci., 50, 2008–2025, https://doi.org/10.1175/1520-0469(1993)050<2008:POTRPO>2.0.CO;2, 1993.

Gelaro, R., McCarty, W., Suárez, M. J., Todling, R., Molod, A., et al.: The modern-era retrospective analysis for research and applications, version 2 (MERRA-2), J. Climate, 30, 5419–5454, https://doi.org/10.1175/JCLI-D-16-0758.1, 2017.

Gayet, J.-F., Ovarlez, J., Shcherbakov, V., Ström, J., Schumann, U., Minikin, A., Auriol, F., Petzold, A., and Monier, M.:
450   Cirrus cloud microphysical and optical properties at southern and northern midlatitudes during the INCA experiment, J. Geophys. Res. Atmos., 109, https://doi.org/https://doi.org/10.1029/2004JD004803, 2004.

Gettelman, A., Fetzer, E. J., Eldering, A., and Irion, F. W.: The Global Distribution of Supersaturation in the Upper Troposphere from the Atmospheric Infrared Sounder, J. Clim., 19, 6089–6103, https://doi.org/10.1175/JCLI3955.1, 2006.

Haag, W., Kärcher, B., Ström, J., Minikin, A., Lohmann, U., Ovarlez, J., and Stohl, A.: Freezing thresholds and cirrus cloud
455   formation mechanisms inferred from in situ measurements of relative humidity, Atmos. Chem. Phys., 3, 1791–1806, https://doi.org/10.5194/acp-3-1791-2003, 2003.

Heymsfield, A. J., Krämer, M., Luebke, A., Brown, P., Cziczo, D. J., Franklin, C., Lawson, P., Lohmann, U., McFarquhar, G., Ulanowski, Z., and Van Tricht, K.: Cirrus Clouds, Meteorol. Monogr., 58, 2.1-2.26, https://doi.org/10.1175/AMSMONOGRAPHS-D-16-0010.1, 2017.

460   Kärcher, B.: Cirrus Clouds and Their Response to Anthropogenic Activities, Curr. Clim. Chang. Reports, 3, 45–57, https://doi.org/10.1007/s40641-017-0060-3, 2017.

Kärcher, B. and Jensen, E. J.: Microscale characteristics of homogeneous freezing events in cirrus clouds, Geophys. Res. Lett., 44, 2027–2034, https://doi.org/https://doi.org/10.1002/2016GL072486, 2017.

Kärcher, B., DeMott, P. J., Jensen, E. J., and Harrington, J. Y.: Studies on the Competition Between Homogeneous and

465   Heterogeneous Ice Nucleation in Cirrus Formation, J. Geophys. Res. Atmos., 127, e2021JD035805, https://doi.org/https://doi.org/10.1029/2021JD035805, 2022.

Krämer, M., Schiller, C., Afchine, A., Bauer, R., Gensch, I., Mangold, A., Schlicht, S., Spelten, N., Sitnikov, N., Borrmann, S., de Reus, M., and Spichtinger, P.: Ice supersaturations and cirrus cloud crystal numbers, Atmos. Chem. Phys., 9, 3505–3522, https://doi.org/10.5194/acp-9-3505-2009, 2009.

470   Liou, K.-N.: Influence of Cirrus Clouds on Weather and Climate Processes: A Global Perspective, Mon. Weather Rev., 114, 1167–1199, https://doi.org/10.1175/1520-0493(1986)114<1167:IOCCOW>2.0.CO;2, 1986.

Liou, K.-N.: Radiation and cloud processes in the atmosphere. Theory, observation, and modeling, New York, NY (United States); Oxford University Press, United States, 1992.

Lohmann, U. and Feichter, J.: Global indirect aerosol effects: a review, Atmos. Chem. Phys., 5, 715–737,
475   https://doi.org/10.5194/acp-5-715-2005, 2005.

Lynch, D. K., Sassen, K., Starr, D. O., and Stephens, G.: Cirrus, Oxford University Press, 2002.

Mace, G. G. and Wrenn, F. J.: Evaluation of the Hydrometeor Layers in the East and West Pacific within ISCCP Cloud-Top Pressure–Optical Depth Bins Using Merged CloudSat and CALIPSO Data, J. Clim., 26, 9429–9444, https://doi.org/10.1175/JCLI-D-12-00207.1, 2013.

480   McGraw, Z., Storelvmo, T., Samset, B. H., and Stjern, C. W.: Global Radiative Impacts of Black Carbon Acting as Ice Nucleating Particles, Geophys. Res. Lett., 47, e2020GL089056, https://doi.org/https://doi.org/10.1029/2020GL089056, 2020.

Montgomery, M. T., Davis, C., Dunkerton, T., Wang, Z., Velden, C., Torn, R., Majumdar, S. J., Zhang, F., Smith, R. K., Bosart, L., Bell, M. M., Haase, J. S., Heymsfield, A., Jensen, J., Campos, T., and Boothe, M. A.: The Pre-Depression
485   Investigation of Cloud-Systems in the Tropics (PREDICT) Experiment: Scientific Basis, New Analysis Tools, and Some First Results, Bull. Am. Meteorol. Soc., 93, 153–172, https://doi.org/10.1175/BAMS-D-11-00046.1, 2012.

Murphy, D. M. and Koop, T.: Review of the vapour pressures of ice and supercooled water for atmospheric applications, Q. J. R. Meteorol. Soc., 131, 1539–1565, https://doi.org/10.1256/qj.04.94, 2005.

O'Shea, S. J., Choularton, T. W., Lloyd, G., Crosier, J., Bower, K. N., Gallagher, M., Abel, S. J., Cotton, R. J., Brown, P. R.
490   A., Fugal, J. P., Schlenczek, O., Borrmann, S., and Pickering, J. C.: Airborne observations of the microphysical structure of two contrasting cirrus clouds, J. Geophys. Res. Atmos., 121, 13,510-513,536, https://doi.org/https://doi.org/10.1002/2016JD025278, 2016.

Ovarlez, J., Gayet, J.-F., Gierens, K., Ström, J., Ovarlez, H., Auriol, F., Busen, R., and Schumann, U.: Water vapour measurements inside cirrus clouds in Northern and Southern hemispheres during INCA, Geophys. Res. Lett., 29, 60–64,

Atmospheric
Chemistry
and Physics
Discussions

495   https://doi.org/https://doi.org/10.1029/2001GL014440, 2002.

Pan, L. L., Bowman, K. P., Atlas, E. L., Wofsy, S. C., Zhang, F., Bresch, J. F., Ridley, B. A., Pittman, J. V, Homeyer, C. R., Romashkin, P., and Cooper, W. A.: The Stratosphere–Troposphere Analyses of Regional Transport 2008 Experiment, Bull. Am. Meteorol. Soc., 91, 327–342, https://doi.org/10.1175/2009BAMS2865.1, 2010.

Pan, L. L., Atlas, E. L., Salawitch, R. J., Honomichl, S. B., Bresch, J. F., Randel, W. J., Apel, E. C., Hornbrook, R. S.,
500   Weinheimer, A. J., Anderson, D. C., Andrews, S. J., Baidar, S., Beaton, S. P., Campos, T. L., Carpenter, L. J., Chen, D., Dix, B., Donets, V., Hall, S. R., Hanisco, T. F., Homeyer, C. R., Huey, L. G., Jensen, J. B., Kaser, L., Kinnison, D. E., Koenig, T. K., Lamarque, J.-F., Liu, C., Luo, J., Luo, Z. J., Montzka, D. D., Nicely, J. M., Pierce, R. B., Riemer, D. D., Robinson, T., Romashkin, P., Saiz-Lopez, A., Schauffler, S., Shieh, O., Stell, M. H., Ullmann, K., Vaughan, G., Volkamer, R., and Wolfe, G.: The Convective Transport of Active Species in the Tropics (CONTRAST) Experiment, Bull. Am.
505   Meteorol. Soc., 98, 106–128, https://doi.org/10.1175/BAMS-D-14-00272.1, 2017.

Patnaude, R. and Diao, M.: Aerosol Indirect Effects on Cirrus Clouds Based on Global Aircraft Observations, Geophys. Res. Lett., 47, e2019GL086550, https://doi.org/10.1029/2019GL086550, 2020.

Patnaude, R., Diao, M., Liu, X., and Chu, S.: Effects of thermodynamics, dynamics and aerosols on cirrus clouds based on in situ observations and NCAR CAM6, Atmos. Chem. Phys., 21, 1835–1859, https://doi.org/10.5194/acp-21-1835-2021,
510   2021.

Pruppacher, H. R. and Klett, J. D.: Microphysics of Clouds and Precipitation, 2nd ed., Springer Netherlands, Dordrecht, 954 pp., https://doi.org/10.1007/978-0-306-48100-0, 2010.

Sassen, K., Wang, Z., and Liu, D.: Global distribution of cirrus clouds from CloudSat/Cloud-Aerosol Lidar and Infrared Pathfinder Satellite Observations (CALIPSO) measurements, J. Geophys. Res., 113, D00A12,
515   https://doi.org/10.1029/2008JD009972, 2008.

Spichtinger, P. and Gierens, K. M.: Modelling of cirrus clouds – Part 2: Competition of different nucleation mechanisms, Atmos. Chem. Phys., 9, 2319–2334, https://doi.org/10.5194/acp-9-2319-2009, 2009.

Stephens, B. B., Long, M. C., Keeling, R. F., Kort, E. A., Sweeney, C., Apel, E. C., Atlas, E. L., Beaton, S., Bent, J. D., Blake, N. J., Bresch, J. F., Casey, J., Daube, B. C., Diao, M., Diaz, E., Dierssen, H., Donets, V., Gao, B.-C., Gierach, M., Green,
520   R., Haag, J., Hayman, M., Hills, A. J., Hoecker-Martínez, M. S., Honomichl, S. B., Hornbrook, R. S., Jensen, J. B., Li, R.-R., McCubbin, I., McKain, K., Morgan, E. J., Nolte, S., Powers, J. G., Rainwater, B., Randolph, K., Reeves, M., Schauffler, S. M., Smith, K., Smith, M., Stith, J., Stossmeister, G., Toohey, D. W., and Watt, A. S.: The O2/N2 Ratio and CO2 Airborne Southern Ocean Study, Bull. Am. Meteorol. Soc., 99, 381–402, https://doi.org/10.1175/BAMS-D-16-0206.1, 2018.

525   Twomey, S.: The Influence of Pollution on the Shortwave Albedo of Clouds, J. Atmos. Sci., 34, 1149–1152,

Atmospheric
Chemistry
and Physics
Discussions

https://doi.org/10.1175/1520-0469(1977)034<1149:TIOPOT>2.0.CO;2, 1977.

Volkamer, R., Baidar, S., Campos, T. L., Coburn, S., DiGangi, J. P., Dix, B., Eloranta, E. W., Koenig, T. K., Morley, B., Ortega, I., Pierce, B. R., Reeves, M., Sinreich, R., Wang, S., Zondlo, M. A., and Romashkin, P. A.: Aircraft measurements of BrO, IO, glyoxal, NO_2, H_2O, O_2–O_2 and aerosol extinction profiles in the tropics: comparison with aircraft-/ship-based
530   in situ and lidar measurements, Atmos. Meas. Tech., 8, 2121–2148, https://doi.org/10.5194/amt-8-2121-2015, 2015.

Wofsy, S. C.: HIAPER Pole-to-Pole Observations (HIPPO): fine-grained, global-scale measurements of climatically important atmospheric gases and aerosols, Philos. Trans. R. Soc. A Math. Phys. Eng. Sci., 369, 2073–2086, 2011.

Zhao, B., Wang, Y., Gu, Y., Liou, K.-N., Jiang, J. H., Fan, J., Liu, X., Huang, L., and Yung, Y. L.: Ice nucleation by aerosols from anthropogenic pollution, Nat. Geosci., 12, 602–607, https://doi.org/10.1038/s41561-019-0389-4, 2019.

535   Zondlo, M. A., Paige, M. E., Massick, S. M., and Silver, J. A.: Vertical cavity laser hygrometer for the National Science Foundation Gulfstream-V aircraft, J. Geophys. Res., 115, D20309, https://doi.org/10.1029/2010JD014445, 2010.

Atmospheric
Chemistry
and Physics
Discussions

Table 1. A list of the funding agency, field campaign name, date, and flight hours at temperatures ≤ -40°C for the seven NSF

540 research campaigns and five NASA campaigns used in this work.

Agency	Field Campaign	Full Name	Year(s)	Spatial Extent	T ≤ -40°C Flight Hours
NSF	CONTRAST	CONvective TRansport of Active Species in the Tropics	2014	20°S – 40°N, 132°E – 105°W	71
	DC3	Deep Convective Clouds and Chemistry Project	2012	25°N – 43°N, 106°W – 79°W	73
	HIPPO*	HIAPER Pole-to-pole Observations	2009 2010 2011	67°N – 87°N, 128°E – 90°W	118
	ORCAS	The O_2/N_2 Ratio and CO_2 Airborne Southern Ocean Study	2016	75°S – 18°S, 91°W – 51°W	41
	PREDICT	PRE-Depression Investigation of Cloud systems in the Tropics	2010	10°N – 29°N, 87°W – 38°W	92
	START08	Stratosphere-Troposphere Analyses of Regional Transport	2008	26°N – 63°N, 117°W – 86°W	55
	TORERO	Tropical Ocean tRoposphere Exchange of Reactive halogen species and Oxygenated voc	2012	42°S – 14°N, 105°W – 70°W	54
NASA	ATTREX	Airborne Tropical TRopopause EXperiment	2014	12°S – 36°N, 134°E – 117°W	128
	MACPEX	Mid-latitude Airborne Cirrus Properties EXperiment	2011	26°N – 41°N, 104°W – 84°W	31
	DC3	Deep Convective Clouds and Chemistry Project	2012	30°N – 42°N, 117°W – 106°W	29
	POSIDON	Pacific Oxidants, Sulfur, Ice, Dehydration, and cONvection	2016	1°S – 15°N, 131°E – 161°E	41
	SEAC4RS	Studies of Emissions and Atmospheric Composition, Clouds and Climate Coupling by Regional Surveys	2013	19°N – 50°N, 80°W – 120°W	15

* Only used deployments #2 to #5.
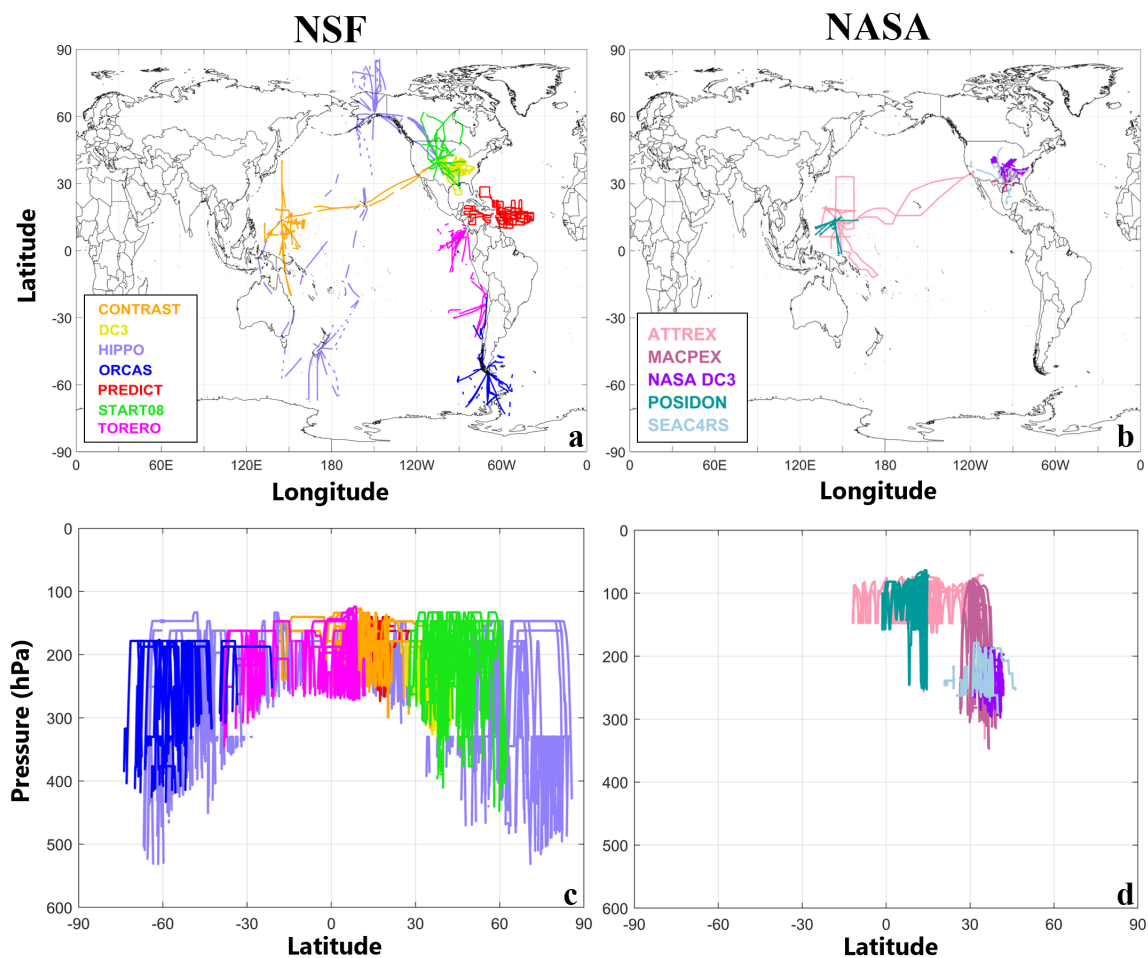
Figure 1. The flight tracks for (a) seven NSF flight campaigns and (b) five NASA campaigns. (c) and (d) show the latitudinal cross-section of the NSF and NASA datasets, respectively. All flight tracks are restricted to temperatures ≤ -40°C.
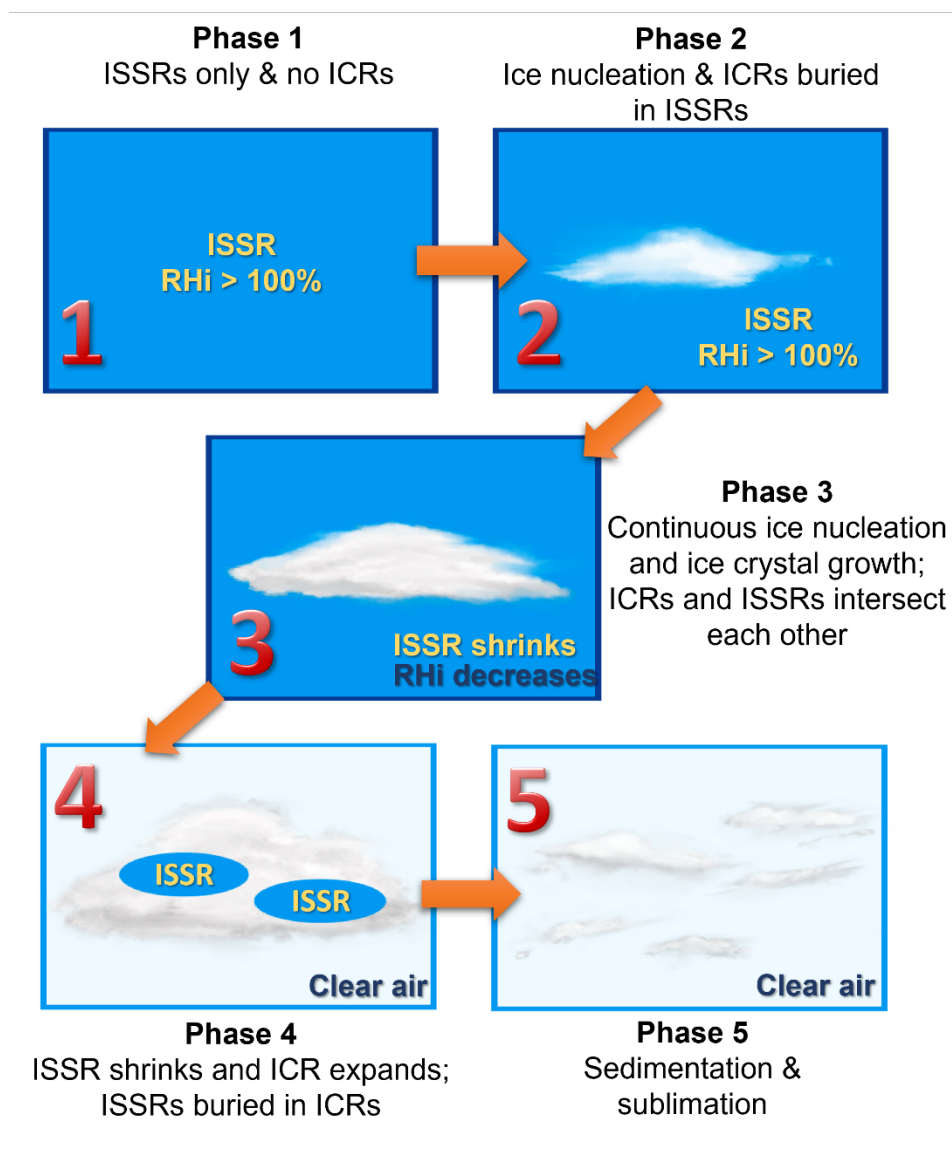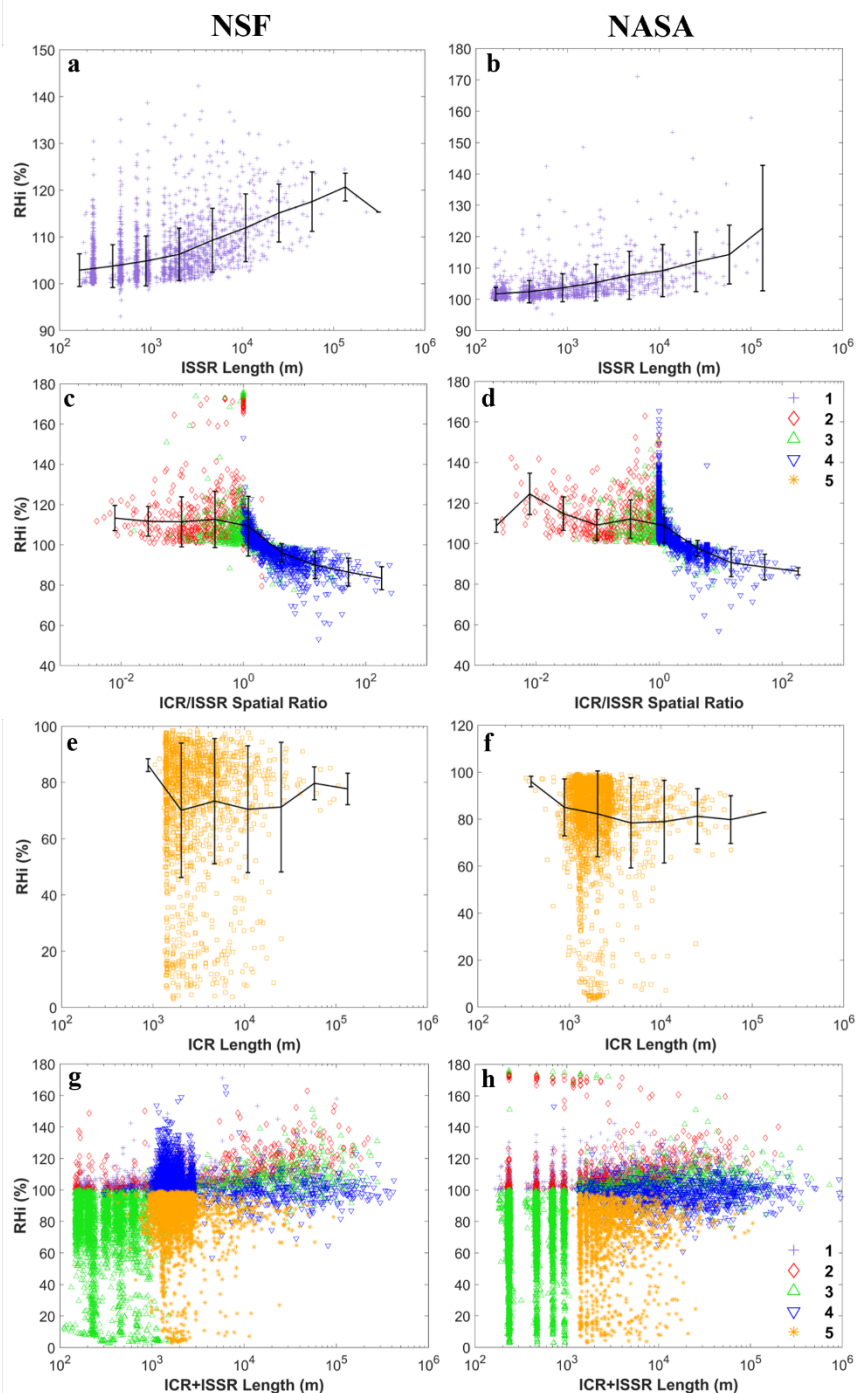
545

Figure 2. An idealized illustration of five cirrus cloud evolution phases as defined in Diao et al. (2013).
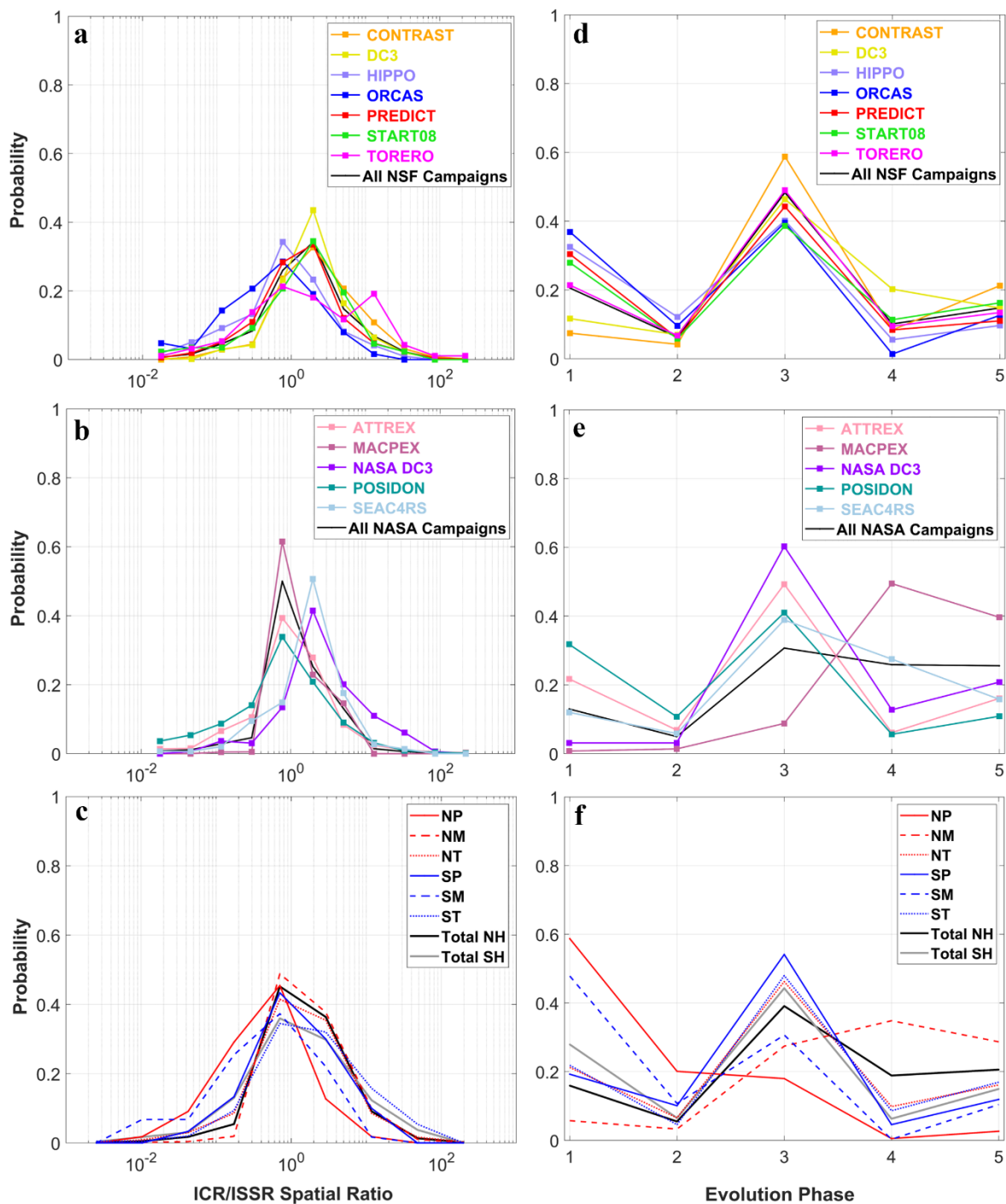
Figure 3. Probabilities of (a-c) the ICR/ISSR spatial ratio and (d-f) five evolution phases for NSF, NASA, and all campaigns in row 1, 2 and 3, respectively. The probabilities are shown for each campaign (in a, b, d and e) and for each latitudinal region 550 (in c and f).

Figure 4. RHi distributions for (a, b) phase 1, (c, d) phases 2 to 4, (e, f) phase 5, and (g, h) all five evolution phases. Observations from NSF and NASA campaigns are shown in column 1 and 2, respectively. All error bars in this and the following figures represent ± one standard deviation.
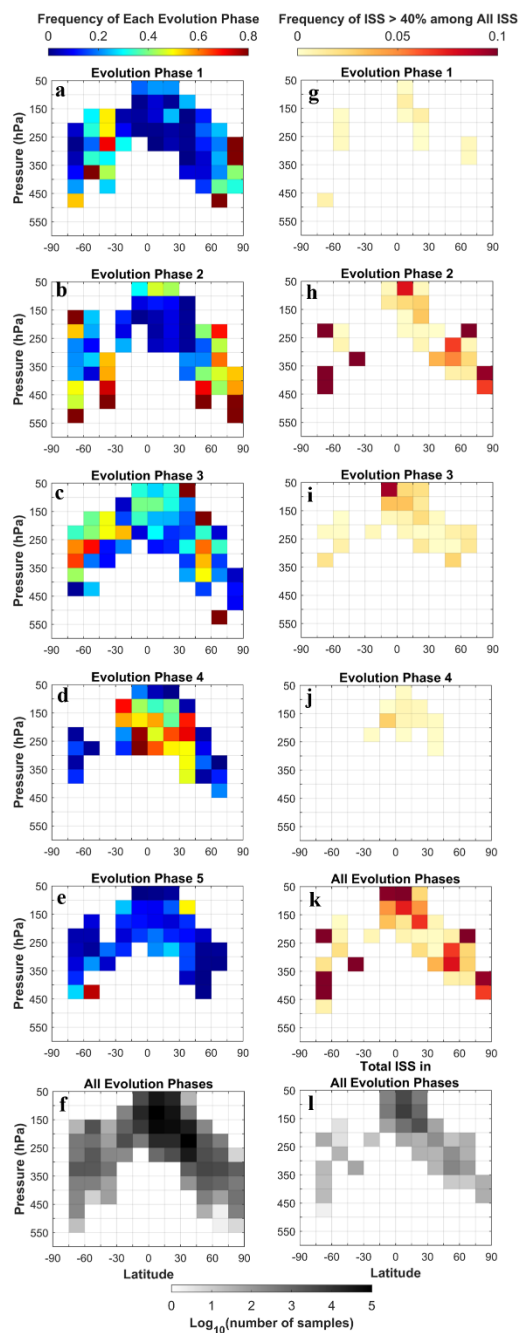
555

Figure 5. The hemispheric distribution of the occurrence frequencies of (a-e) each evolution phase and (g-k) RHi > 140% among all ice supersaturated conditions in each phase. (f) Number of samples for five evolution phases. (l) Number of samples for all ISS conditions in five phases. This analysis is based on combined NSF and NASA datasets
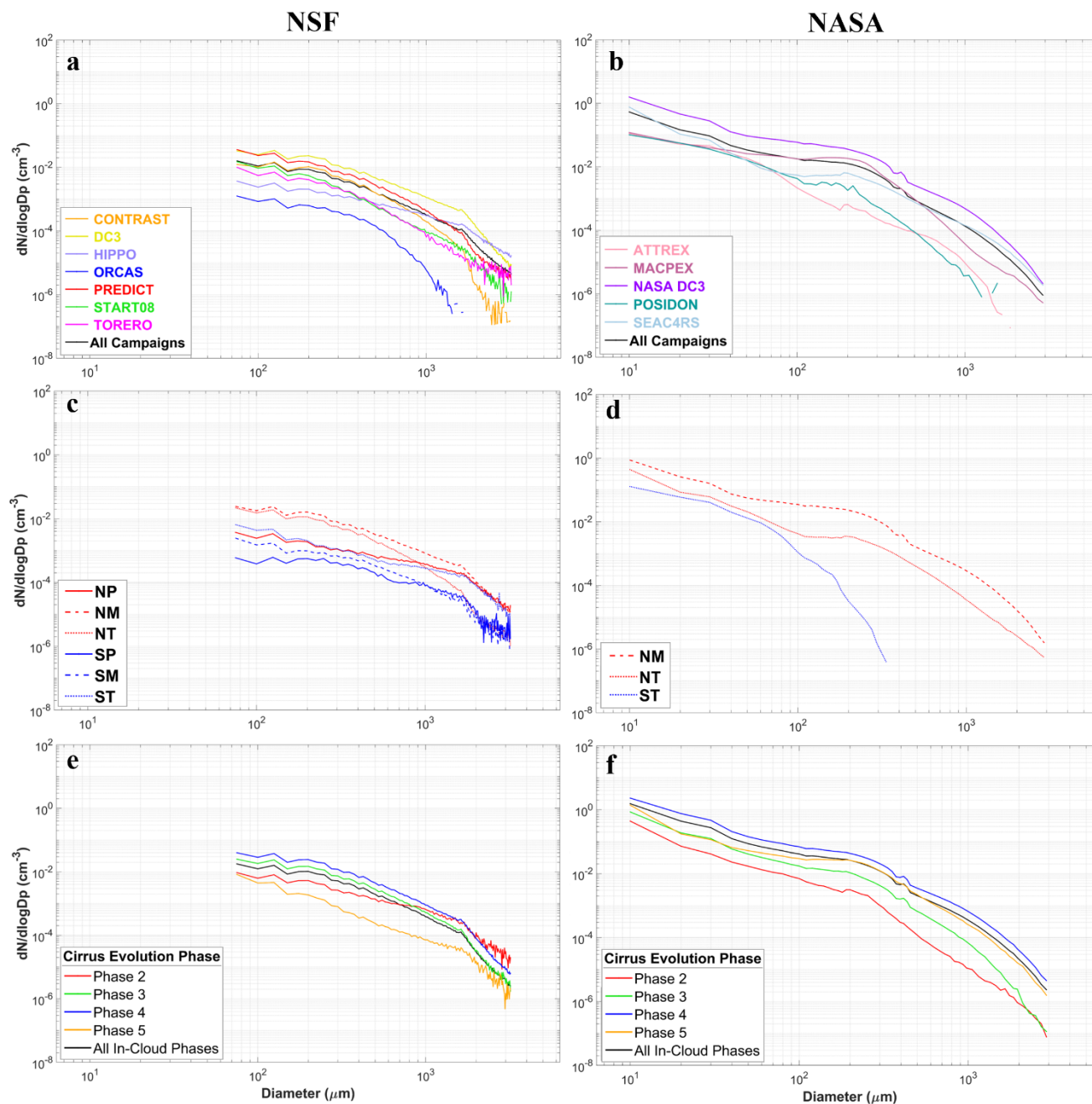
Figure 6. Particle size distribution plots using (a, c and e) the 2DC cloud probe for NSF campaigns and (b, d, and f) 2DS probe for NASA campaigns. The data are separated by (a, b) campaigns, (c, d) latitudinal regions, and (e, f) the cirrus cloud evolution phases. dN/dlogDp is the average particle number concentration in each bin normalized by the log10 scale bin width.
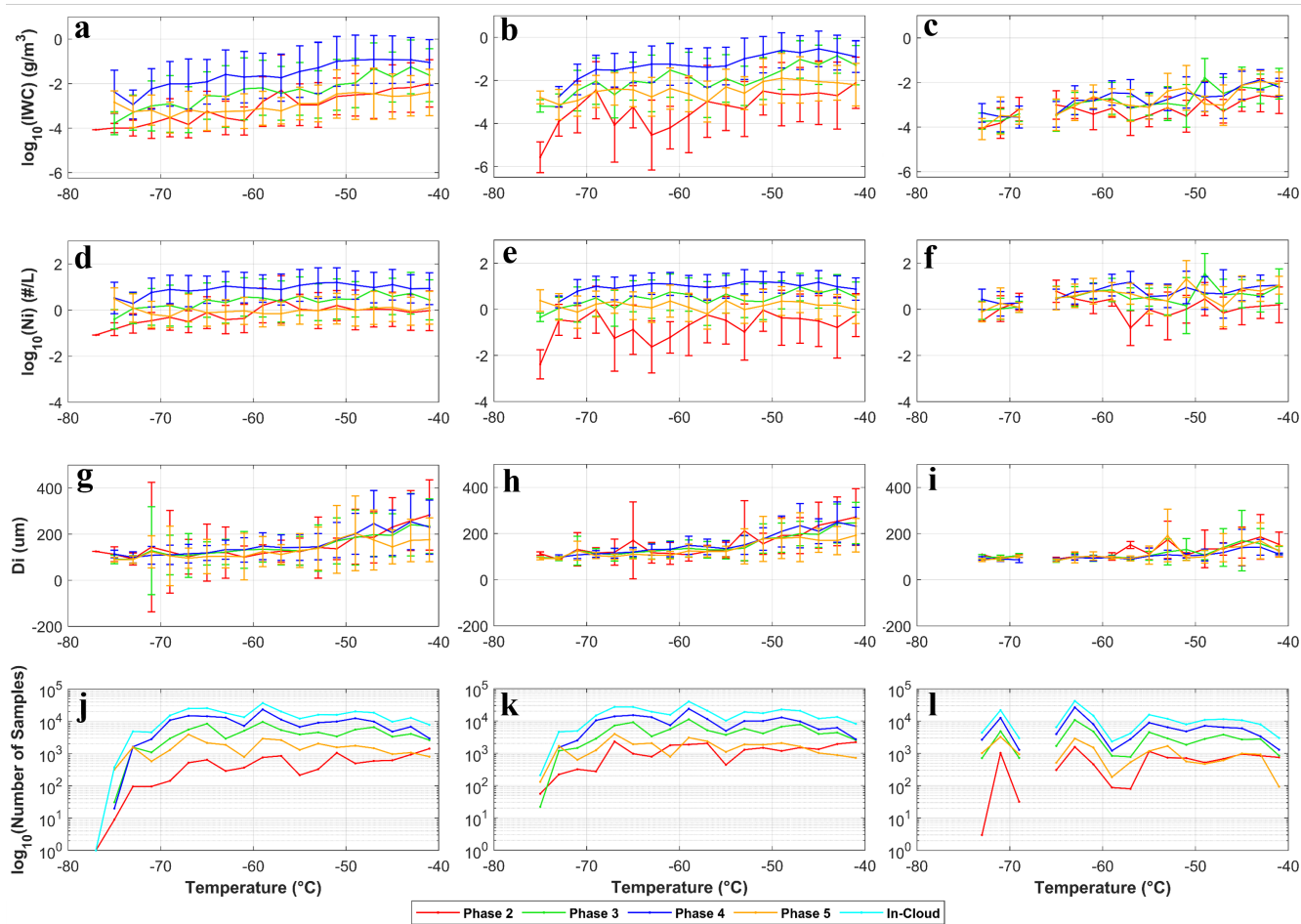
Figure 7. Averages of $\log_{10}$(IWC), $\log_{10}$(Ni), and Di in each 2-degree temperature bin for evolution phases 2 to 5 using 1-s observations, 430-s observations, and the simulations in column 1, 2 and 3, respectively. The number of samples is shown in the last row. In Figures 7 – 15, only NSF campaigns are used for comparisons with model simulations.
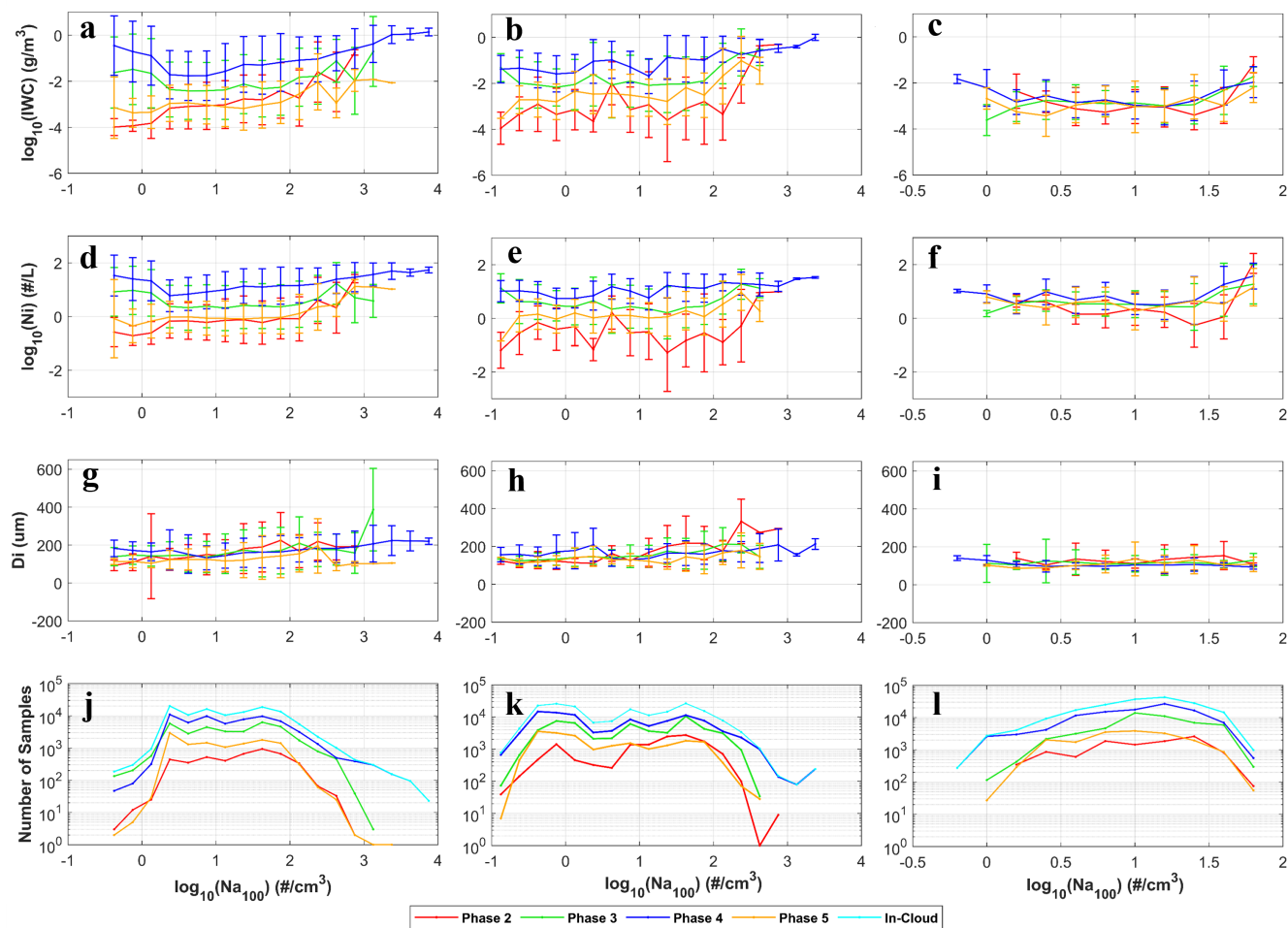
**Figure 8.** Similar to Figure 7, except for plotting cloud microphysical properties against $\log_{10}(Na_{100})$.

570
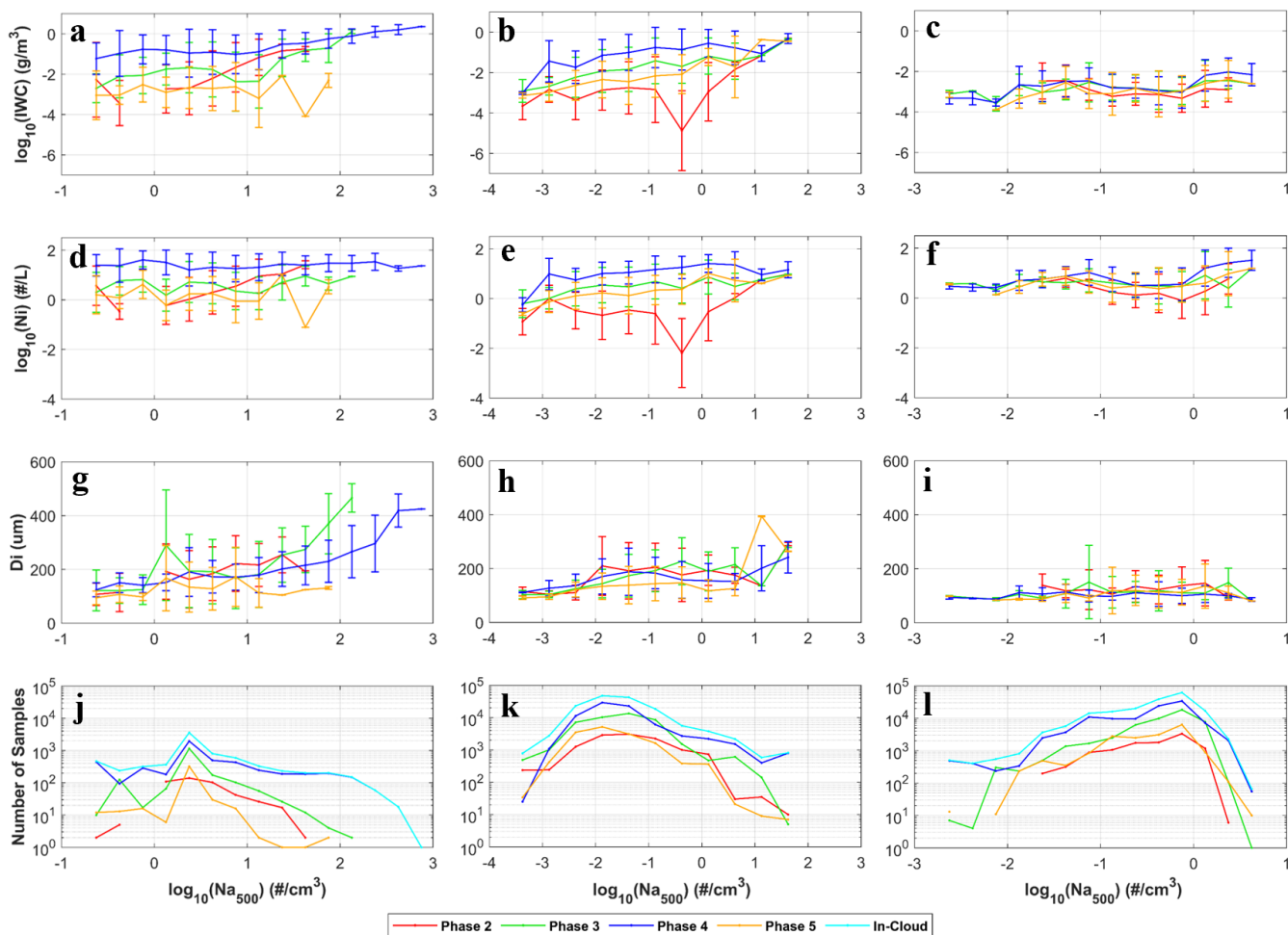
**Figure 9.** Similar to Figure 8, except for plotting cloud microphysical properties against $\log_{10}(Na_{500})$.
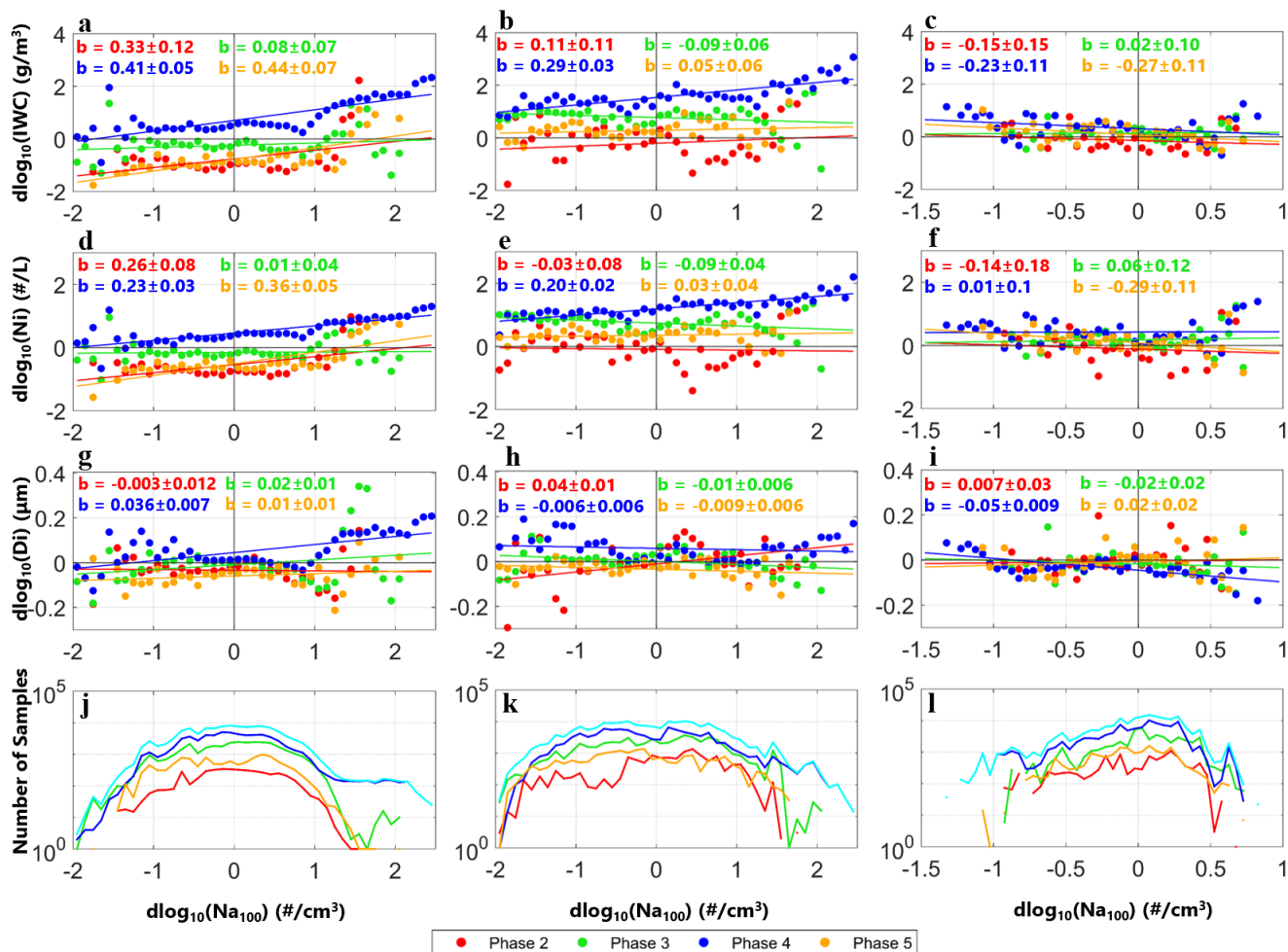
Figure 10. Linear regressions of the delta values of cirrus microphysical properties, i.e., $d\log_{10}(IWC)$, $d\log_{10}(Ni)$, and $d\log_{10}(Di)$ with respect to $d\log_{10}(Na_{100})$ for evolution phases 2 to 5 (various colored lines). Columns 1, 2 and 3 represent 1-s observations, 430-s observations, and simulations, respectively. The slope value and its standard deviation are shown for each linear regression. The number of samples is shown in the last row.
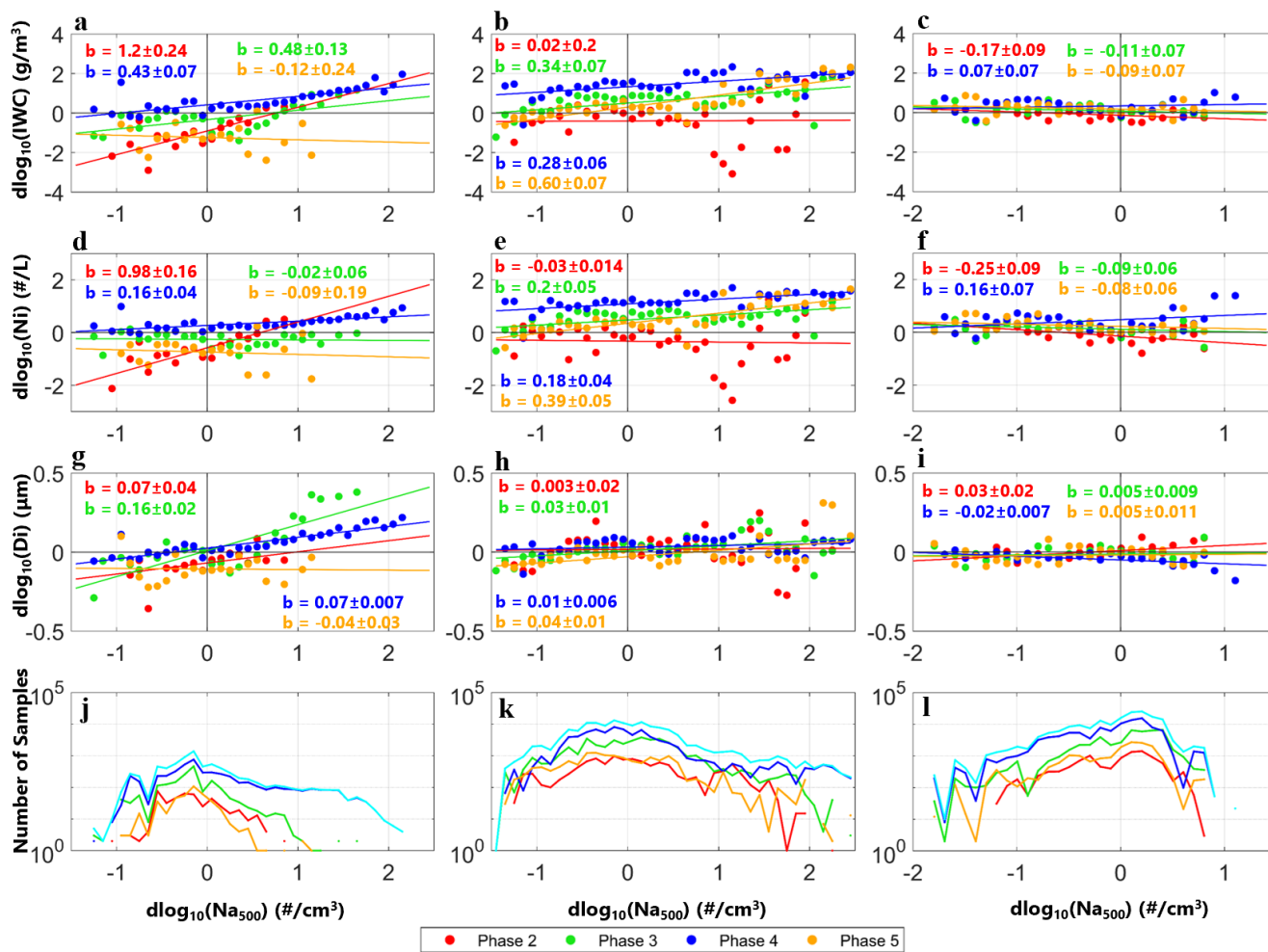
Figure 11. Similar to Figure 10, except for linear regressions with respect to $dlog_{10}(Na_{500})$.
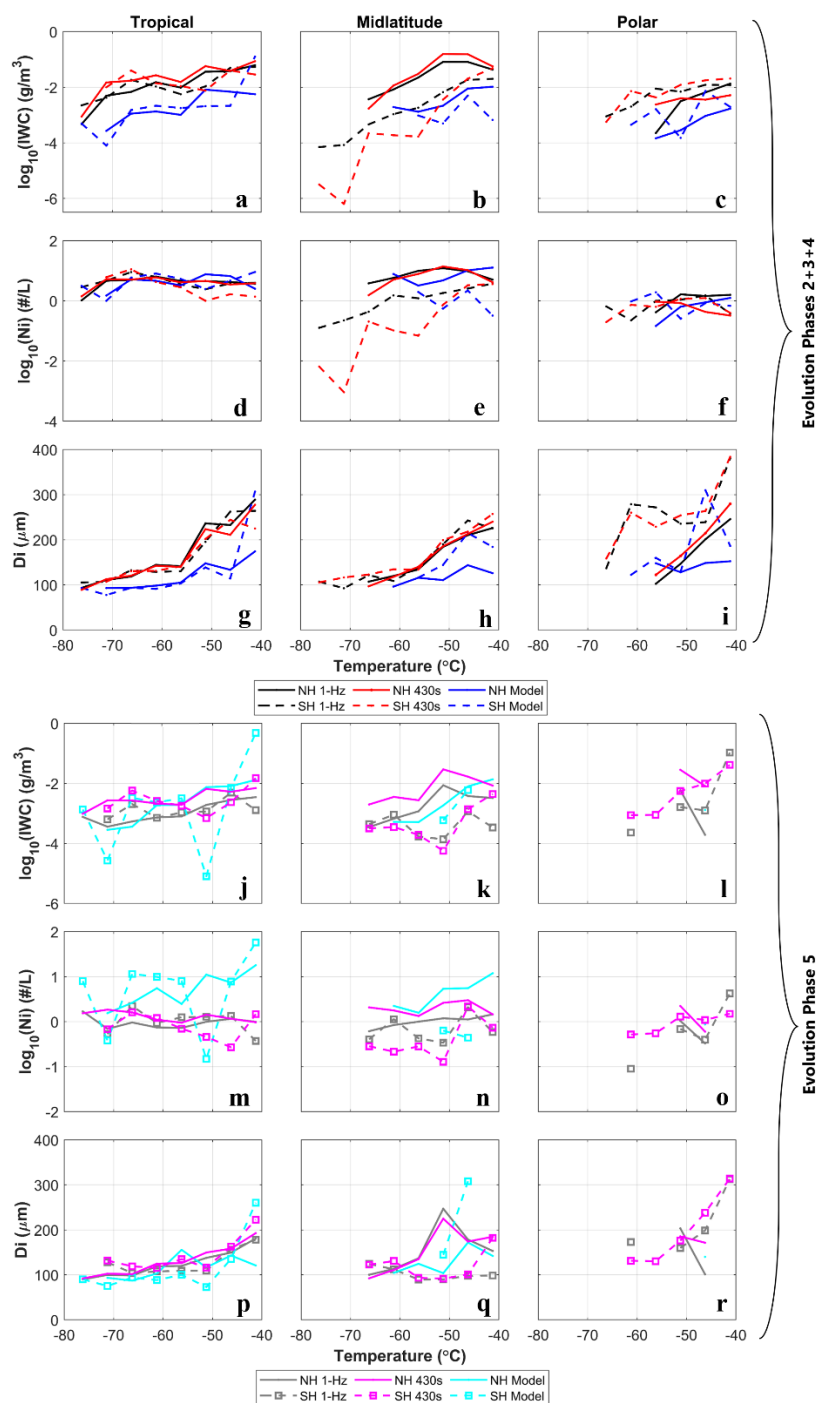
**Figure 12.** Averages of $\log_{10}(IWC)$, $\log_{10}(Ni)$, and Di for every 5-degree temperature bin for evolution phases 2 to 5, separated by NH and SH. The top three rows are for phases 2+3+4 while the bottom three rows are for phase 5 only. The number of samples is shown in the supplementary material (Figure S2).
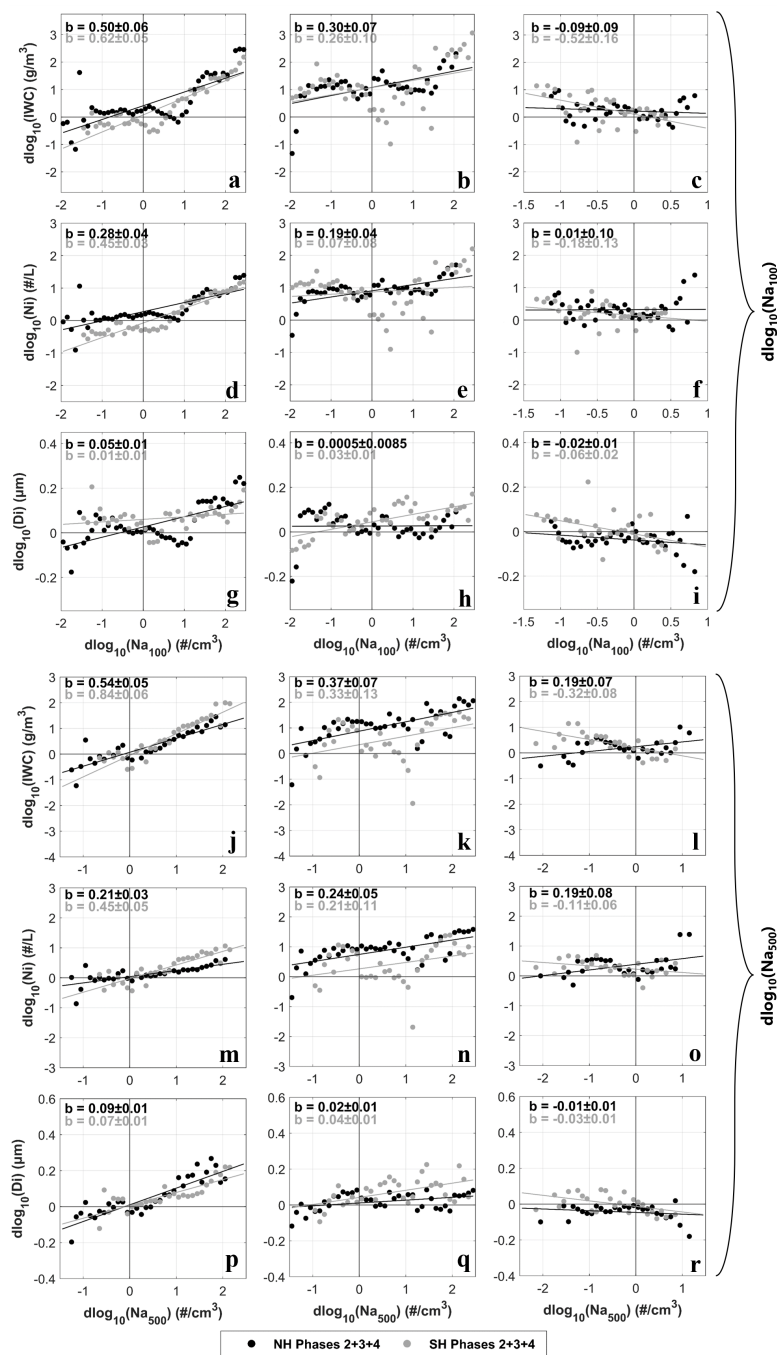
585

Figure 13. Linear regression of $\log_{10}(IWC)$, $\log_{10}(Ni)$, and Di with respect to the aerosol number concentrations, (top three rows) Na_{100} and (bottom three rows) Na_{500}. This analysis shows the combined phases 2, 3 and 4, separated by NH and SH. The number of samples is shown in the supplementary material (Figure S3).
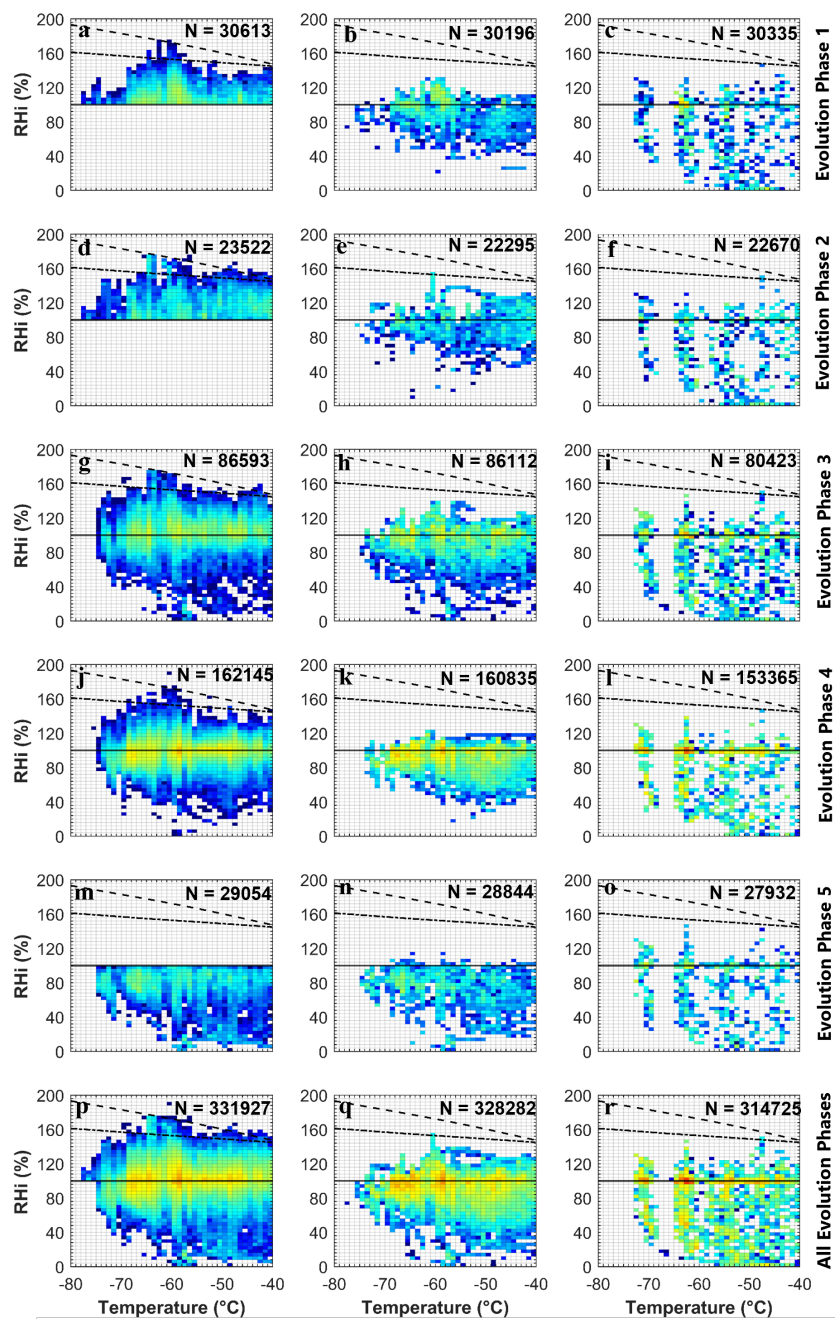
Figure 14. Distributions of RHi in relation to temperature for five evolution phases shown for 1-s observations, 430-s observations and simulations in column 1, 2 and 3, respectively. Number of samples (in seconds) is shown in logarithmic scale. The solid line represents ice saturation while the dashed line represents liquid saturation. The dot-dashed line shows the homogeneous nucleation threshold for aerosols with a size of 0.5 μm.

Atmospheric
Chemistry
and Physics
Discussions
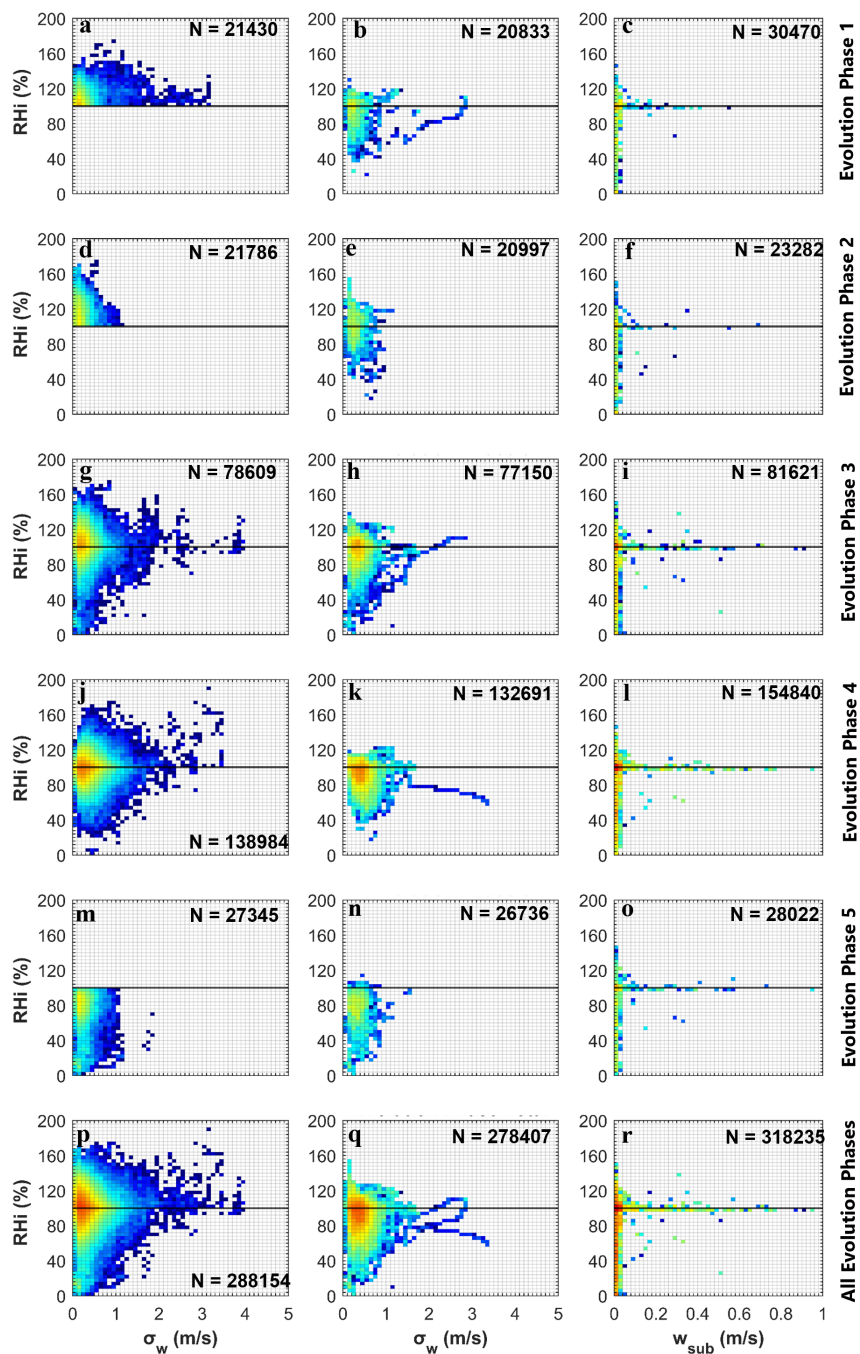
Figure 15. Similar to Figure 14, except for distributions of σ_w in relation to temperature.